Submitted to Physical Review C

LBL-6521
Preprint C.1

MICROSCOPIC CALCULATIONS OF HIGH-SPIN ROTATIONAL STATES

Chin W. Ma and John O. Rasmussen

May 1977

Prepared for the U. S. Energy Research and Development Administration under Contract W-7405-ENG-48

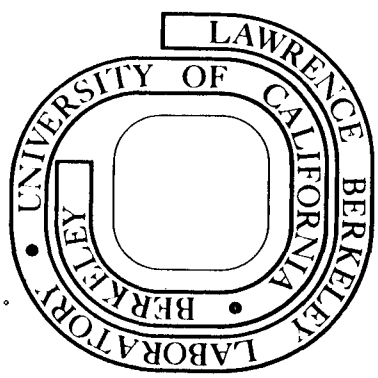

DISCLAIMER

Microscopic Calculations of High-Spin Rotational States*

Chin W. Ma

Cyclotron Institute and Physics Department, Texas A&M University, College Station, Texas 77843

and

John O. Rasmussen

Lawrence Berkeley Laboratory, University of California, Berkeley, California 94720

Abstract

The high-spin rotational states of ^{162}Er, ^{168}Yb, ^{174}Hf, and ^{238}U are calculated microscopically by diagonalizing the cranking Hamiltonian $H-\omega J_x$ using both BCS and fully particle-number projected wave functions. The computational effort in the latter case is greatly reduced due to a newly derived compact formula for the residuum integral. The results show that pairing collapse does not occur in all four nuclei up to spin 20. The moderate increase of the moment-of-inertia at low spin is due to both higher-order cranking and Coriolis-anti-pairing effects. The crossing of the decoupled two quasi-particle band with the ground band is responsible for the rapid increase of the moment-of-inertia at high spin. The present calculations are able to produce the rotational energies fairly well in general, but the Nilsson single-particle levels have to be adjusted in order to reproduce the backbending behavior in ^{162}Er.

[NUCLEAR STRUCTURE calculated high-spin rotational states by diagonalizing cranking model. New formula for particle-number projection. g_R factor, backbending, Coriolis-anti-pairing and rotational alignment effects.]

1. Introduction

The energy spaciing of the high-spin nuclear rotational states, especially the backbending behavior, has been an interesting subject for many experimental and theoretical studies in recent years.[1] The rapid increase of the moment-of-inertia at high spin which causes a reversal of the monotonic increase in level spacing (backbending) to happen in some nuclei is considered generally to be the result of the crossing of the ground band with an excited band of large moment-of-inertia whose real nature is still a question of debate. There exist now several microscopic Hartree-Fock-Bogoliubov (HFB) calculations which either are based on the cranking model[2-5] or use angular momentum projection.[6] The general consensus of these studies is that the two most important factors which cause the nuclear moment-of-inertia to rapidly increase are the rotational alignment effect[7] and the Coriolis anti-pairing (CAP) effect.[8] The quantitative results of these studies for particular nuclei, however, can be quite different. For instance, some calculations may obtain pairing collapse while others do not.

In the present paper we shall study the high-spin rotational states by diagonalizing the cranking Hamiltonian $H-\omega J_x$. Our diagonalization method resembles the Coriolis matrix diagonalization approach of Stephens and Simon[7] except that we start with a microscopic Hamiltonian with pairing correlation as variation parameters, whereas they use the rotor plus particle model with pairing fixed. The microscopic nature of the present calculation makes it possible to study the different competing effects, for example, the rotational alignment effect, the CAP effect, etc. in a self-consistent way. BCS wave functions in some cases and fully particle-number projected (FBCS) wave functions in others are used in the present

calculations to study the fixed-particle-number correction for high-spin states.

The rotational spectra of ^{162}Er, ^{168}Yb, ^{174}Hf, and ^{238}U are calculated. Experimentally, ^{162}Er shows backbending while the other three do not. We discuss the diagonalization method in section 2 and the particle-number projection in section 3. The detailed calculations and the results are presented in sections 4 and 5. Section 6 gives the conclusions.

2. Diagonalization of the cranking equation

We start with the cranking equation

$$(H-\omega J_x)\Psi(\omega)=W(\omega)\Psi(\omega) \quad , \tag{2.1}$$

where ω is the angular velocity which is related to the angular momentum I by the constraint

$$\langle\Psi(\omega)|J_x|\Psi(\omega)\rangle=\sqrt{I(I+1)} \quad . \tag{2.2}$$

The Hamiltonian H is chosen to be identical to that of Nilsson et al.[9], who included the Nilsson single-particle Hamiltonian plus a pairing interaction.

$$H=\sum_{k>0}\varepsilon_k(c_k^+c_k+c_{\bar{k}}^+c_{\bar{k}})-G\sum_{k,p>0}c_k^+c_{\bar{k}}^+c_{\bar{p}}c_p \quad , \tag{2.3}$$

where c_k^+ and c_k are the particle creation and annihilation operator respectively; k is the I_z component along the nuclear symmetric axis, G is the pairing strength, and the time-reversed state is defined as

$$|\bar{k}\rangle=(-1)^{k-\frac{1}{2}}|-k\rangle \quad .$$

We first carry out the Bogoliubov-Valatin quasi-particle transformation

$$\alpha_k^+=U_kc_k^+-V_kc_{\bar{k}} \quad , \tag{2.4}$$

with

$$U_k^2 + V_k^2 = 1 \quad .$$

The H and the J_x operators can be expressed in terms of these quasi-particle operators as[10]

$$H = H_{00} + H_{11} + H_{20} + H_{22} + H_{31} + H_{40} \tag{2.5}$$

$$J_x = (J_x)_{11} + (J_x)_{20} \quad . \tag{2.6}$$

The cranking equation (2.1) can then be solved by expanding $\Psi(\omega)$ in this quasi-particle representation

$$\Psi(\omega) = \sum_{\tau, n\geq 0} a_{n\tau} |\tilde{n}, \tau\rangle \quad , \tag{2.7}$$

where n denotes the number of quasi-particles, and τ stands for all other appropriate quantum numbers. For example,

$$|\tilde{2}, ij\rangle = \alpha_i^+ \alpha_j^+ |\tilde{0}\rangle \quad ,$$

where $|\tilde{0}\rangle$ is the quasi-particle vacuum state

$$|\tilde{0}\rangle = \prod_{k>0} (U_k + V_k c_k^+ c_{\bar{k}}^+) |0\rangle \tag{2.8}$$

In the BCS approximation the ground state is the vacuum $|\tilde{0}\rangle$, and the rotational excited states are obtained by mixing the quasi-particle states $|\tilde{n}, \tau\rangle$ with the vacuum through the Coriolis interaction ωJ_x. For low-spin rotational states, the ωJ_x term is small and second order perturbation treatment should be sufficiently good.[10] In the intermediate-spin region (I~10) one can perform fourth-order perturbation calculations.[11] As the spin becomes even higher, however, the mixing of the quasi-particle becomes so strong that one probably should avoid the perturbation treatment and rely on the diagonalization method. Indeed, in the remaining

text we shall use the diagonalization approach to study the high-spin rotational spectrum.

2.1 Choice of truncated space

In order to choose a reasonable truncated space in the expansion (2.7), we notice first that the Hamiltonian in Eq. (2.3) does not contain proton-neutron pairing; thus, the proton part and the neutron part can always be treated separately. In addition, the J_x term does not mix different parity states; thus, if we neglect the quasi-particle interaction terms and consider $H_{00} + H_{11} - \omega J_x$ only, the wave function $\Psi(\omega)$ can be expressed as a product

$$\Psi(\omega) = |P+\rangle |P-\rangle |N+\rangle |N-\rangle \ ,$$

where $|P+\rangle$ and $|P-\rangle$ (or $|N+\rangle$ and $|N-\rangle$) denote the proton (or neutron) positive-parity and negative-parity orbital subspace respectively.

We next note that four-quasi-particle contributions to the rotational states are unimportant until the spin becomes very high.[7] Hence, in the present calculations we shall consider only the two-quasi-particle excitations in each orbital subspace. The wave function can now be written explicitly as

$$\begin{aligned}\Psi(\omega) = &\Big[a_0(P+) + \sum_{\lambda,j}^{P+} a_{\lambda j}(P+)\,\alpha_\lambda^+ \alpha_j^+\Big]\Big[a_0(P-) + \sum_{\lambda,j}^{P-} a_{\lambda j}(P-)\,\alpha_\lambda^+ \alpha_j^+\Big] \\ &\times \Big[a_0(N+) + \sum_{\lambda,j}^{N+} a_{\lambda j}(N+)\,\alpha_\lambda^+ \alpha_j^+\Big]\Big[a_0(N-) + \sum_{\lambda,j}^{N-} a_{\lambda j}(N-)\,\alpha_\lambda^+ \alpha_j^+\Big]|\tilde{0}\rangle ,\end{aligned} \tag{2.9}$$

with

$$W(\omega) = H_{00} + \sum_\tau W_\tau(\omega) \ , \tag{2.10}$$

where τ = P+, P-, N+, and N-. The amplitude $a_0(\tau)$, $a_{ij}(\tau)$ and the values of w_τ can be determined by the following equation

$$\left[H^{\tau}_{11} - \omega J_x^{\tau} \right] \psi_\tau(\omega) = w_\tau(\omega) \psi_\tau(\omega) \quad , \tag{2.11}$$

where

$$\psi_\tau(\omega) = \left[a_0(\tau) + \sum_{i,j}^{\tau} a_{ij}(\tau) \alpha_i^\dagger \alpha_j^\dagger \right] |\tilde{0}\rangle \quad . \tag{2.12}$$

Thus diagonalization can now be carried out separately for each subspace; this greatly simplifies our calculations. In the remaining text, the script τ (or P+, P-, N+ and N-) will be omitted whenever possible, provided there will be no ambiguity.

2.2 Coriolis anti-pairing effect

The coefficient $\{U_k, V_k\}$ of the canonical transformation (2.4) will now be determined by the minimization

$$\delta \langle \Psi(\omega) | H - \omega J_x | \Psi(\omega) \rangle = 0 \quad , \tag{2.13}$$

with respect to $\{U_k, V_k\}$. The trial wave function $\Psi(\omega)$ is given in Eq. (2.9) obtained from the separate diagonalizations.

We choose to reduce the number of variational parameters by constraining the $\{U_k, V_k\}$ to have the BCS form with ν a free variational parameter

$$\left.\begin{matrix} U_k^2 \\ V_k^2 \end{matrix}\right\} = \frac{1}{2} \left[1 \pm \frac{\varepsilon_k - \lambda}{\left[(\varepsilon_k - \lambda)^2 + \nu^2 \right]^{\frac{1}{2}}} \right] \quad . \tag{2.14}$$

Therefore, the set of variables $\{U_k, V_k\}$ is reduced to a single variable ν. We remark here that for $\omega = 0$, the trial wave function $\Psi(\omega)$ of (2.9) reduces to the quasi-particle vacuum $|\tilde{0}\rangle$, and ν becomes the BCS gap parameter

$$\Delta = G \sum_{k>0} U_k V_k \quad . \tag{2.15}$$

In general, however, ν is a function of ω, and our calcuations show that the value of ν decreases as ω increases, which is simply a manifestation of the CAP effect.

The chemical potential λ in Eq. (2.14) is adjusted for each angular velocity ω so that the average particle number is conserved, namely

$$\langle \Psi(\omega) | \hat{N} | \Psi(\omega) \rangle = n \quad , \tag{2.16}$$

where $\hat{N}$ is the particle number operator. Note that for each value of ω we obtain a set of $\nu_p(\omega)$ and $\lambda_p(\omega)$ for protons and a set of $\nu_n(\omega)$ and $\lambda_n(\omega)$ for neutrons. Thus for each ω one obtains a new set of quasiparticle basis functions

$$\alpha_k^+(\omega) = U_k(\omega)\, c_k^+ - V_k(\omega)\, c_{\bar{k}} \quad . \tag{2.17}$$

The wave function in the new basis, however, can be expressed in terms of the uncranked basis [Eq. (2.4)]. For example, the quasiparticle vacuum in the new basis

$$|\tilde{0}\rangle_\omega = \prod_{k>0} \left(U_k(\omega) + V_k(\omega)\, c_k^+ c_{\bar{k}}^+ \right) |0\rangle$$

is a superposition of quasiparticle pairs in the uncranked basis α_k^+, namely

$$|\tilde{0}\rangle_\omega = \prod_{k>0} \left(A_k + B_k\, \alpha_k^+ \alpha_{\bar{k}}^+ \right) |\tilde{0}\rangle \quad ,$$

where

$$A_k = U_k U_k(\omega) + V_k V_k(\omega)$$

$$B_k = U_k V_k(\omega) - V_k U_k(\omega) \quad .$$

Therefore, the use of a new set of $\{U_k(\omega), V_k(\omega)\}$ for each cranking velocity ω does effectivly admix 4, 6, etc. quasiparticle states in the uncranked basis and makes our truncation to 0 and 2 quasiparticle states in the cranked basis more justifiable.

2.3 The quasi-particle interaction

The previous discussions have omitted any interaction between quasi-particle. We shall now describe how to include them partially. Let us first consider the H_{20} term. For non-zero ω, ν does not equal Δ, the BCS equation no longer holds and H_{20} does not vanish. It is straightforward, however, to include H_{20} in our calculation for arbitrary value of ν. Next, the H_{22} term can couple a quasi-particle pair in orbit p with another pair in orbit q, where orbitals p and q are of opposite parity. Likewise H_{40} can create two pairs, one in orbit p and the other in orbit q. Therefore, strictly speaking, the full inclusion of H_{22} and H_{40} will make it impossible for us to diagonalize the cranking equation separately. For simplicity, we shall neglect the above couplings. Their contributions are estimated to be small, because for non-zero ω, the Coriolis interaction ωJ_x will excite essentially the unpaired states.

To summarize, we shall include in addition to H_{00} and H_{11} the quasi-particle interaction terms given in Eq. (2.5) except that they are restricted to act only between orbits with the same parity. For example, we shall include those H_{22} terms that couple one quasi-particle pair in orbit p with another pair in orbit q, provide orbitals p and q are of the same parity. We are thus led to solve the following equations

$$\left[\mathcal{H}^{\tau} - \omega J_x^{\tau} - \lambda_\tau \hat{N}_\tau\right] \psi_\tau(\omega) = w_\tau(\omega)\, \psi_\tau(\omega) \quad , \tag{2.18}$$

where $\mathcal{H} = H - H_{00}$, $\lambda_{P+} = \lambda_{P-} = \lambda_p$, $\lambda_{N+} = \lambda_{N-} = \lambda_n$ and $\psi(\omega)$ is given by Eq. (2.12). The total energy of the rotational state is

$$E(\omega) = H_{oo} + \sum_\tau w_\tau(\omega) + \omega \langle \Psi(\omega) | J_x | \Psi(\omega) \rangle + \sum_\tau \lambda_\tau \langle \psi_\tau(\omega) | \hat{N} | \psi_\tau(\omega) \rangle \quad , \tag{2.19}$$

with

$$\langle \Psi(\omega) | J_x | \Psi(\omega) \rangle = \sum_\tau \langle \psi_\tau(\omega) | J_x | \psi_\tau(\omega) \rangle \ . \qquad (2.20)$$

Note that we have introduced a Lagrange multiplier term $\lambda \hat{N}$ in (2.18) to take care of the average particle number relation (2.16). The results obtained by solving Eqs. (2.18)-(2.20) are labeled as the BCS calculation. As it turns out, the inclusion of the quasi-particle interactions does make the calculated results better.

3. Calculations with particle-number projection

The wave functions given by eqns. (2.9) and (2.12) do not conserve particle number. The study of Rich[12] shows that the particle-number fluctuations will cuase a 10% to 20% error in cranking calculations of low-lying rotational states. Recent Hartree-Fock-Bogoliubov (HFB) calculations show that the effect of particle-number fluctuations may become very important in the study of backbending phenomenon. For example, Dalafi et al.[13] show that a not fully self-consistent HFB cranking model calculation using BCS wave functions will not reproduce backbending in ^{168}Er, while calculation with approximate number-projection will. The same group later found, however, that a fully self-consistent calculation will reproduce backbending in ^{162}Er even without number projection[2]. Another example is provided by Faessler et al.[14]; they have applied the partial number-projection method first suggested by Sorensen[15] in their HFB calculations and found that calculation without number-projection will not reproduce backbending in ^{166}Yb while calculation with two-point number-projection will. Later it was reported that an improved calculation[16] with four-point number-projection fails

again to reproduce the backbending. In this section we shall discuss how to apply the fully number-projected wave function with variation after projection (FBCS) to solve the cranking equation.

The normalized projected BCS ground and two quasi-particle states can be expressed as[17]

$$\phi_0 = \frac{1}{(R_0^0)^{\frac{1}{2}}} \frac{1}{2\pi i} \oint d\zeta \frac{1}{\zeta^{n_0+1}} \prod_{k>0} (U_k + \zeta V_k c_k^+ c_{\bar{k}}^+) |0\rangle \tag{3.1}$$

$$\phi_{p\bar{p}} = \frac{1}{[R_1'(p) + R_0'(p) - R_0^0]^{\frac{1}{2}}} \frac{1}{2\pi i} \oint d\zeta \frac{1}{\zeta^{n_0+1}} (\zeta U_p c_p^+ c_{\bar{p}}^+ - V_p) \times \prod_{k\neq p} (U_k + \zeta V_k c_k^+ c_{\bar{k}}^+) |0\rangle \tag{3.2}$$

$$\phi_{pq} = \frac{1}{(R_1^2(p,q))^{\frac{1}{2}}} \frac{1}{2\pi i} \oint d\zeta \frac{\zeta}{\zeta^{n_0+1}} c_p^+ c_q^+ \prod_{k\neq p,q} (U_k + \zeta V_k c_k^+ c_{\bar{k}}^+) |0\rangle, \tag{3.3}$$

where $2n_0$ is the number of particles. The residuum integrals R_n^N appearing in eqns. (3.1)-(3.3) are defined as

$$R_n^N(\nu_1 \cdots \nu_N) = \frac{1}{2\pi i} \oint d\zeta \frac{\zeta^n}{\zeta^{n_0+1}} \prod_{k\neq \nu_1 \cdots \nu_N} (U_k^2 + \zeta V_k^2) . \tag{3.4}$$

They can be evaluated by the recursion relations given in Ref. 17. In a realistic calculation, however, the computation of R_n^N is very time consuming, and it becomes one of the main handicaps in using the FBCS wave functions.

We were able to derive a formula which expressed R_n^N in terms of R_0^0 and $R_0^1(i)$ as (see appendix)

$$R_n^N(\nu_1 \cdots \nu_N) = \delta_{nN} R_0^0 \prod_{i=\nu_1 \cdots \nu_N} \frac{1}{V_i^2} + (-1)^n \sum_{i=\nu_1 \cdots \nu_N} V_i^{2(N-n-1)} U_i^{2n} \left(\prod_{\substack{k=\nu_1 \cdots \nu_N \\ \neq i}} \frac{1}{V_i^2 - V_k^2} \right) R_0'(\nu_i) \tag{3.5}$$

This enables the expression of quantities calculated with the projected wave functions in terms of $\{U_i\}, \{V_i\}, \{R_0^1(i)\}$ and R_0^0. As a result, the computational effort of a specific FBCS calculation only increases by about 20% over that of the BCS one. However, in the present BCS calculation the chemical potential λ has to be adjusted for each angular velocity ω; this in fact makes the BCS calculation as a whole more time-consuming than the FBCS one.

In terms of these projected bases, the calculations of the proton part can still be separated from that of the neutron part. Thus considering only the proton (or neutron) part, one can project the total wave function of (2.9) term by term and obtain

$$\Phi_P(\omega) = a_0(P+)\,a_0(P-)\,\phi_0 + a_0(P+)\sum_{i,j}^{P-} a_{ij}(P-)\,\phi_{ij}$$
$$+ a_0(P-)\sum_{i,j}^{P+} a_{ij}(P+)\,\phi_{ij} + \sum_{i,j}^{P+}\sum_{p,q}^{P-} a_{ij}(P+)\,a_{pq}(P-)\,\phi_{ijpq} \qquad (3.6)$$

where ϕ_{ijpq} is the normalized projected four-quasi-particle wave function.

Unlike the BCS case, the cranking equation cannot be solved separately in the psoitive- and negative-parity orbital subspaces, even if the quasi-particle interactions between different parity orbits are neglected. In order to do so, the following approximateions are thus made.

a. In writing down the secular equation of eq. (2.1) using the projected wave function (3.6), the non-orthogonality relations among the ground state ϕ_0 and the pair states $\{\phi_{k-k}\}$ are only partially applied.

b. All quasi-particle interactions are neglected. That is, only the diagonal matrix element of the Hamiltonian

$$\mathcal{H} = H - \langle\phi_0|H|\phi_0\rangle \qquad (3.7)$$

are taken into account.

c. The following relations which hold in the the BCS representation are assumed to be also true in the FBCS case, e.g.

$$\langle \phi_{ij} | J_x | \phi_{ijpq} \rangle = \langle \phi_o | J_x | \phi_{pq} \rangle$$

$$\langle \phi_{ijst} | J_x | \phi_{ijpq} \rangle = \langle \phi_{st} | J_x | \phi_{pq} \rangle$$

$$\langle \phi_{ij} | \phi_{ijk-k} \rangle = \langle \phi_o | \phi_{k-k} \rangle \quad .$$

Using the above approximation, the FBCS cranking equation can then be diagonalized separately in the four orbital subspaces, namely

$$[\mathcal{H} - \omega J_x] \phi_\tau(\omega) = W_\tau \phi_\tau(\omega) \tag{3.8}$$

$$\phi_\tau(\omega) = a_o(\tau) \phi_o + \sum_{i,j}^{\tau} a_{ij}(\tau) \phi_{ij} \quad , \tag{3.9}$$

where τ = P+, P-, N+, and N-; $\mathcal{H}$ is given in (3.7). The total energy of the rotational state is

$$E(\omega) = \langle \phi_o | H | \phi_o \rangle + \sum_\tau W_\tau(\omega) + \omega \langle \Phi(\omega) | J_x | \Phi(\omega) \rangle \tag{3.10}$$

with

$$\langle \Phi(\omega) | J_x | \Phi(\omega) \rangle = \sum_\tau \langle \phi_\tau(\omega) | J_x | \phi_\tau(\omega) \rangle \quad . \tag{3.11}$$

The results obtained by solving (3.8)-(3.11) are labeled as the FBCS calculations.

4. Detailed Calculations

The deformed single-particle basis used in the present calculations is chosen to be identical to that of Nilsson et al.[9] Our treatment

of pairing interaction strength is also identical to theirs, namely

$$G_A = g_0 \pm g_1 \frac{N-Z}{A}$$
$$g_0 = 19.2\ \text{MeV}, \quad g_1 = 7.4\ \text{MeV}, \tag{4.1}$$

with plus sign for protons and minus sign for neutrons. The BCS equations are then solved by including $(15Z)^{1/2}$ or $(15N)^{1/2}$ states above and below the protron or neutron Fermi level.

All two-quasi-particle states $|ij\rangle$ with zero-order energies

$$\left[(\varepsilon_i - \lambda_{BCS})^2 + \Delta_{BCS}^2\right]^{\frac{1}{2}} + \left[(\varepsilon_j - \lambda_{BCS})^2 + \Delta_{BCS}^2\right]^{\frac{1}{2}} \leq 0.8\hbar\omega_0 \tag{4.2}$$

are included in our truncated space for rare-earth nuclei, where ε_i is the Nilsson single-particle energy; λ_{BCS}, Δ_{BCS} are respectively the chemical potential and the gap parameter obtained from the BCS calculation. In the case of actinide nuclei, the truncation is taken to be $0.75\hbar\omega_0$. In fact, we have varied the truncated energy from $0.7\hbar\omega_0$ to $1.2\hbar\omega_0$ and found that the results differ by only 1%.

The cranking equation will now be diagonalized separately in the four two-quasi-particle subspaces P+, P-, N+ and N-. It is interesting to note, however, that even in each of the subspaces, the $H-\omega J_x$ matrix can be further reduced to block form, provide the following bases are used, namely[18]

$$|\mu_1 k_1, \mu_2 k_2\rangle_\pm \equiv \frac{1}{\sqrt{2}}\left[|\mu_1 k_1, \mu_2 k_2\rangle \pm |\mu_2 -k_2, \mu_1 -k_1\rangle\right], \quad \mu_1 \neq \mu_2 \tag{4.3}$$

$$|\mu_1 k_1, \mu_1 -k_1\rangle_\pm \equiv |\mu_1 k_1, \mu_1 -k_1\rangle$$

where k is the I_z component, μ is the labeling of the orbit. In order to avoid double counting of the two-quasi-particle states, one has $k_1 > 0$, $k_1 + k_2 \geq 0$; and $\mu_1 > \mu_2$ if $k_1 = k_2$.

The vacuum $|\tilde{0}\rangle$ and the states $\{|\mu_1 k_1, \mu_2 k_2\rangle_+\}$ then form the symmetric subspace $\|+\}$ which is decoupled from the anti-symmetric subspace $\|-\}$ spanned by the states $\{|\mu_1 k_1, \mu_2 k_2\rangle_-\}$. That is

$$\{+\| H - \omega J_x \|-\} = 0$$

Since we are interested only in the lowest few eigenstates of the cranking equation, we can confine the present calculations to the symmetric subspace because the solutions of the anti-symmetric subspace which does not include the vacuum state in general lie higher. Thus, the size of the $H-\omega J_x$ matrix is now reduced by nearly half. For example, using the two quasi-particle truncation of (4.2), the largest dimension of the $H-\omega J_x$ matrix of the N+ orbital subspace is about 200 x 200 for rare-earth nuclei and it is about 300 x 300 for actinide nuclei. However, since the non-zero J_x off-diagonal matrix elements occur mainly along the vicinity of the diagonal line, the diagonalization can be carried out quite fast.

The matrix elements of $H-\omega J_x$ using BCS basis are well known; those using FBCS basis will be given in the appendix.

Before we end this section, two remarks are in order. First, we mention that in the BCS calculation the ground state is treated on the same footing as the excited states. That is, the cranking equation (2.18) is diagonalized at $\omega = 0$ and the pairing parameter ν_0 (BCS) is obtained by minimizing the energy equation (2.19). In the FBCS calculation the pairing parameter ν_0 (FBCS) of the ground state is obtained by minimizing the

ground-state energy (B 1), where U_i, V_i are again given by eqn. (2.14). The pairing strength g_0 of the FBCS calculation is chosen so that the value of ν_0(FBCS) approximately equals the pairing gap parameter Δ_{BCS}, and the lowest 2^+ state of FBCS calculation approximately equals that of the BCS one. Thus, we found

g_0(FBCS) = 18.0 MeV for the A $\sim$ 165 region

g_0(FBCS) = 17.5 MeV for the A $\sim$ 187 and the A $\sim$ 242 region.

Second, we notice that the projected ground state ϕ_0 and the pair states $\{\phi_{k-k}\}$ are not orthogonal among themselves. Thus, we have adopted a method described by Kumar and Baranger [19] which can be used to diagonalize a matrix in a representation spanned by non-orthogonal basis. This method is especially suitable for solving the $H - \omega J_x$ matrix, the off-diagonal matrix elements of which are mostly zero.

5. Results and Discussion

The present calculations have been applied to four nuclei, ^{162}Er, ^{168}Yb, ^{174}Hf and ^{238}U. The experimental specturm of ^{162}Er shows back-bending while the other three do not.[20,21,22]

The values of the quadrupole and hexadecapole deformations taken from Nilsson et al,[9] together with the calculated ground-state pairing parameters ν_0(BCS) and ν_0(FBCS) of the four nuclei, are given in table I. The energies E are plotted as a function of I(I+1) in Fig. 1 to Fig. 4, where I is the spin. The dashed curve represents the BCS calculation without Coriolis-antipairing (CAP) effect, the dotted curve represents the same calculation with CAP effect, the dotted curve represents the FBCS calculation also with CAP effect. The dash-dot curve is the regular cranking result.

5.1 Results of diagonalization

We first discuss the result of pure diagonalization, that is of the calculation performed at ν_0(BCS) without taking into account the CAP effect and particle-number fluctuation. One immediately notices in Fig. 1 to Fig. 4 the significance of diagonalization in calculating the high spin state. For example, the second-order perturbation calculation will produce a straight line in the E~I(I+1) plot, represented by the dash-dot curve. It is seen that diagonalization alone is able to improve the agreement substantially. This indicaes that the deviation from the I(I+1) rule in fact comes mainly from the higher-order cranking terms, which are now taken into account through diagonalization. Recall that we constrain the deformation to be constant.

Let us now analyze the structure of the wave function of the rotational state. For this purpose the vacuum amplitude $a_0(\tau)$ in eq. (2.9) is plotted as a function of I in Fig. 5, where τ = P+, P-, N+ and N-. We notice first that for the rare-earth nuclei, a_0(P+) and a_0(N-) stay close to unity up to spin I~14. This is because the configuration mixing depends strongly on the matrix elements of ωJ_x between states near the chemical potential λ. A look at the Nilsson diagram reveals that no high-j and low-Ω orbits of P+ or N- types lie close to the chemical potential of the rare-earth nuclei, where j and Ω are the angular momentum and its z-component of the singel-particle orbit. Hence, the J_x matrix elements and consequently the configuration mixing are small. The situation is quite different for the N+ and P- solutions. Let us consider ^{162}Er for example. The proton chemical potential lies near the 7/2[523] state of the 1h 11/2 orbit. Since the neighboring states have large values of Ω, the J_x matrix elements are still relatively small, thus, the

configuration mixing becomes important only around spin I~14. The neutron chemical potential, on the other hand, lies near the 3/2[651] state of the li13/2 orbit, therefore large configuration mixing occurs already around spin I~10. The N+ solution at high spin contains mainly two-quasi-particle excitations in the li 13/2 orbits. The two neutron quasi-particles are nearly decoupled after spin I~14 as can be seen from Fig. 6, where the value of $\langle J_x \rangle$ of each solution is plotted as a function of spin I. In the case of ^{162}Er it is seen from Fig. 6 that $\langle J_x \rangle$ of the N+ solution reaches about 10 around spin I~14 and increases very slowly thereafter. On the other hand, roughly speaking, the P+, P-, N- solutions are dominated by the vacuum state with only a small amount of quasi-particle admixture. Thus, the product of the P+, P-, and N- solutions can be considered to represent a rotating core.

The solutions of ^{168}Yb and ^{174}Hf show a similar trend. In the case of ^{238}U and P- and N+ solutions remain quite pure up to spin 18, the P+ solution begins to have large two-quasi-particle mixing around spin I~14. This is because the proton chemical potential now lies near the 3/2 [651] state of the li 13/2 orbit. The two proton quasi-particles become nearly decoupled after spin I~20. The N- solution on the other hand, will not become strongly mixed until spin I~18. Thus, the core is now represented by the P-, N+ and N- solutions. Therefore, although we did not use the rotor-particle model, the present calculation shows this picture is basically correct, provided one keeps in mind that the concept of an inert core with constant moment-of-inertia becomes increasingly inaccurate beyond spin 14 in the case of rare-earth nuclei and beyond spin 18 in the case of ^{238}U.

The very different natures of the N+ solutions of ^{162}Er at low spin, dominated by the vacuum component, and that at high spin, dominated by the two decoupled quasi-particles, are actually the results of band-crossing. In order to illustrate this, the vacuum amplitude a_0(N+) of the second lowest solution n = 2 of ^{162}Er as well as that of the n = 1 solution are plotted as a function of angular velocity ω in Fig. 7. It is interesting to see that the two solutions actually cross each other. That is , the overlap with the ground state of the n = 2 solution is larger than that of the n = 1 solution after ω~0.28. Similar crossing also happens in ^{168}Yb and ^{174}Hf. In the case of ^{238}U, it is seen from Fig. 7 that the first two P+ solutions cross after ω~0.22.

We next study the effective moment-of-inertia defined by

$$\langle J_x \rangle = \omega \mathcal{J} \tag{5.1}$$

The ratio of $\mathcal{J}$ obtained by diagonalization to that obtained by second-order perturbation (ordinary cranking) are plotted in Fig. 8. For the purpose of comparision both results are calculated in the BCS approximation omitting the quasi-particle interaction and evaluated at Δ_{BCS}. The small configuration mixing of the P+ and N- solutions of the three rare-earth nuclei indicates that their moments-of-inertia should change only slightly as the spin increases. This is indeed true as can be seen from Fig. 8, where the values of the above-mentioned ratio are all close to one.

The moment-of-inertia $\mathcal{J}$ of the P- solution of ^{162}Er near I~18 and that of the N+ solution near I~8 both show moderate increase (by a factor of 2). This can be attributed to the moderate amount of two

quasi-particle excitations due to higher-order cranking in the solutions near these spin values. On the other hand, the large increase of $\mathcal{J}$ of the N+ solution around spin I~14 (by a factor of 6) has a different origin, the band-crossing. As we have discussed above, the structure of the yrast state after crossing is very different from that before crossing, thus causing the large increase in the apparent moment-of-inertia. Similar trends of $\mathcal{J}$ for the P- and N+ solutions also occur in ^{168}Yb and ^{174}Hf, except now the maximal increase of $\mathcal{J}$ is by a factor of 4 (see Fig. 8). In the case of ^{238}U, the moments-of-inertia $\mathcal{J}$ of the P- and N+ solutions change very little up to spin 24. There is a moderate increase of $\mathcal{J}$ (by a factor of 2) of the N- solution around spin I~24 and of the P+ solution around spin I~10 due to higher-order cranking. There also appears a large increase of $\mathcal{J}$ of the P+ solution (by a factor of 7) around spin 20 because of band-crossing.

Another quantity of interest is the collective gyromagnetic ratio g_R, which can be expressed approximately as

$$g_R \simeq \frac{\mathcal{J}_p}{\mathcal{J}_p + \mathcal{J}_n} \tag{5.2}$$

where $\mathcal{J}_p$ and $\mathcal{J}_n$ are the moment-of-inertia of the proton part and neutron part, respectively. We have neglected the spin contribution in eq. (5.2) which amounts to about 10%.[23] The $\mathcal{J}_p$ and $\mathcal{J}_n$ are calculated by eq. (5.1), the results for the rare-earth nuclei and that of ^{238}U are plotted as a function of spin I in Fig. 9. It is interesting to see that the g_R factor behaves quite differently in the two cases. For rare-earth nuclei, the g_R factor decreases first up to spin around 12 and then gradually increases. The behavior of g_R is just the opposite

for ^{238}U; there the g_R factor first increases up to spin around 18 and then decreases. The reason is the following: in the case of rare-earth nuclei the large two-quasi-particle mixing in the N+ solution causes $\mathcal{J}_n$ to increase while $\mathcal{J}_p$ stays about the same. After spin 12 the increase of $\mathcal{J}_n$ levels off and $\mathcal{J}_p$ begins to increase, thus leading g_R to decrease first and then increase. In the case of ^{238}U, however, the large configuration mixing in the P+ solution causes $\mathcal{J}_p$ to increase first, thus reversing the behavior of g_R.

5.2 Coriolis-antipairing effect

The calculated energy which takes into account the CAP effect is represented by the dotted curves in Fig. 1 to Fig. 4. Although the CAP effect always improves the results by lowering the energy by about 0.2 MeV to 0.3 MeV for high-spin states, it is not the main source of the rapid increase of the moment-of-inertia at high spin.

The proton and neutron pairing parameters ν_p and ν_n are plotted as dotted curves as functions of spin I in Fig. 10. In the case of rare-earth nuclei, the neutron ν_n first decreases to half its ground-state value at spin around 12 and then stays about the same up to spin 18. The proton pairing parameter ν_p also decreases but at a slower rate. It does not decrease seriously until around spin 14 and even at spin 18, 70% of the proton pairing still remains. In the case of ^{238}U, the proton pairing decreases at a faster rate than neutron pairing; in both cases, however, 50% of the pairing still remains at spin 22.

The attenuation of pairing is closely related to the two-quasi-particle mixing in high-spin states. In the case of rare-earth nuclei, for example, the neutron orbits of positive-parity become rapidly blocked

as the amount of the unpaired two-quasi-particle excitations in the N+ solution increases. This blocking of orbits thus curtails the pairing effect. At spin around 12, the neurtron orbits of postive-parity are essentially blocked causing the neutron pairing to reduce by half. Any further weakening of pariing must now come from the blocking of the neutron orbits of negative parity. But the small configuration mixing of the N- solution indicates that the N- orbits are largely unblocked up to spin 18, leading to the fact that the neutron pairing stays almost unchanged from spin 12 to spin 18. It will diminish again when the quasi-particle excitations in the N- solutions become large which of course will eventually happen at very high spin. Our present calculations, however, indicate that there is no pairing collapse up to spin 20 for rare-earth nuclei. The reduction of proton pairing can be understood in similar way. For example, its slower rate of reduction is due to the fact that configuration mixing in the proton wave function is quite small until around spin 14. After that the two-quasi-particle excitations rapidly increase and the proton pairing also diminishes accordingly.

The CAP effect in ^{238}U follow similar trend, except now the large two-quasi-particle mixing in the P+ solution causes the proton pairing to decrease at a faster rate than the neutron pairing.

In the HFB calculations of Ref. 2 the pairing in the high-j orbitals subject to decoupling falls more rapidly with spin than for other orbitals. Our simplifying assumption of eqn. (2.14) contrains pairing to be about the same in all orbitals, and thus our variational solutions would not be as low in energy as those with all V_k as variational parameters. Both the HFB [2] and our calculations agree that there is not a general pairing collapse

in the backbending or near backbending region.

We shall now study the influence of the CAP effect on the moment-of-inertia $\mathcal{J}$. For this purpose we extract $\mathcal{J}$ from the calculated energies by the standard formula

$$\frac{2\mathcal{J}}{\hbar^2} = \frac{4I - 2}{\Delta E(I \to I-2)}$$

The values of the ratio $(\mathcal{J}_I - \mathcal{J}_2)/\mathcal{J}_2$ obtained from diagonalization alone (the dotted curve) and that obtained from the full calculation (the solid curve) are plotted as a function of spin I in Fig. 11. Only the results of ^{162}Er and ^{174}Hf are given for illustration. The dotted curve represents the fractional increment of the moment-of-inertia $\mathcal{J}$ at spin I over that at spin 2 due to diagonalization without CAP, so the difference between the solid curve and the croresponding dotted curve represents the fractional increment due to the CAP effect. It is seen that the CAP effect and the higher-order cranking both contribute importantly to the slow increase of the moment-of-inertia $\mathcal{J}$ at low spin $I \lesssim 8$. However, the rapid increase of $\mathcal{J}$ at high spin is maily due to the crossing of the decoupled band, as we have discussed in the last section. Here the CAP effect only plays a minor role.

In the aboye discussion the meaning of CAP effect is restricted to a narrow sense; that is if the pairing parmeter is kept fixed at ν_0, we consider the calculation made without CAP effect. This is not true in a broad sense. For example, the decoupling of two neutron quasi-particles in the li 13/2 orbit at constant ν_0 does imply a decrease in the pairing

field

$$\langle F \rangle = \langle G \sum_{k>0} c_k^+ c_{\bar{k}}^+ \rangle \ .$$

Using the BCS solution (2.9), the expectation value of the pairing field operator for neutron can be written as

$$\langle F_n \rangle = \Delta_n - G \sum_{\lambda}^{N+,N-} (-1)^{\Omega_\lambda - \frac{1}{2}} a_0 \, a_{\lambda,-\lambda} (V_\lambda^2 - U_\lambda^2)$$
$$- G \sum_{\lambda,\,j}^{N+,N-} |a_{\lambda j}|^2 (U_\lambda V_\lambda + U_j V_j) \ , \qquad (5.3)$$

and a similar expression for proton. In the case of ^{162}Er, for calculations with fixed pairing parameters ν_{on} and ν_{op} given in table I, $\langle F_n \rangle$ decreases from 0.92 MeV at ground state to 0.81 MeV at spin I = 18; and $\langle F_p \rangle$ decreases from 0.94 MeV at ground state to 0.90 MeV at I = 18, since the two-quasi-particle admixture in the latter case is much smaller. For calculations including CAP effect the values of ν and $\langle F \rangle$ differ by less than 5%. This is because Δ is larger than ν in general, the difference Δ-ν increases as ν reduces, this partially cancels the negative contributions of the second and third terms in eqn. (5.3).

Finally, we want to mention that the increase of neutron pairing after spin 12 in ^{168}Yb accompanies a fall in proton pairing and rise in proton moment-of-inertia. The results of the FBCS calculation do not show this behavior.

5.3 Results of Particle-number Projection

The results of FBCS calculations with the inclusion of CAP effect are plotted as solid curve in Fig. 1 to Fig. 4. In general the FBCS results are slightly better than the BCS ones. It is interesting to see that the

fixed-particle-number correction does not change appreciably as the excitation energy increases. Thus, the BCS approximation is quite reliable even for high-spin states where substantial quasi-particle excitations are present in the wave functions. The FBCS calculations also give a somewhat smaller CAP effect than that given by the BCS ones, as can be seen in Fig. 10, where the FBCS calculations are represented by the solid curves. For example, the nuetron pairing parameter ν_n and the proton pairing parameter ν_p have still about 70% of the ground-state values at spin around 18.

5.4 Backbending in ^{162}Er

The present calculations are able to reproduce the energies of the high-spin rotational states quite well without introducing any free parameter. However, we can reproduce actual reversal in the monotonic increase of rotational level spacing (backbending) in ^{162}Er only by shifting the Nilsson single-particle levels. In this section we shall discuss this problem in detail.

It was pointed out by Sorensen[1] that the exact treatment of cranking formalism without angular momentum projection will not produce backbending. This failure is attributed to the fact that large spreading in $\langle J_x \rangle$ will occur in the cranking solution at the band crossing region, thus smoothing out the backbending effect. Recently, Hamamoto[24] showed that HFB calculations without self-consistency, that is, in which the pairing field is kept constant for all values of ω, are also unable to produce backbending for the same reason. But a detailed study by Sorensen on the two-level pairing model[25] does demonstrate that if the self-consistency of pairing is properly taken into account, the HFB calculation will reduce the spreading in $\langle J_x \rangle$ and consequently produce the backbending behavior, although in realistic case the HFB calculation may be less accurate in the backbending

region as was pointed out by Chu et al.[26]

The present method of diagonalization show similar features. According to the general arguments of Sorensen,[1] diagonalization of the cranking equation (2.1) alone without taking into account the CAP effect will not produce backbending. The reason is that for each value of ω only the lowest soltuion of $W(\omega)$ of eqn. (2.1) corresponds to the yrast state, since the eigenvalue curve $W(\dot{\omega})$ as a function of the parameter ω will not cross itself (the "no crossing" rule); therefore there will be only one yrast state for each ω, and backbending will not occur. However, in addition to diagonalization, we also treat the pairing self-consistently,i.e. for each value of ω the pairing parameter ν is varied after diagonalization to study the CAP effect. Although our treatment is not fully self-consistent in the sense that we do not vary all V_k but only ν. Nevertheless, one may now obtain two or more minima of $\delta\langle H-\omega J_x\rangle = 0$ at different values of ν for a given ω, wich make it possible for backbending to occur. Note that the eigenvalues at the different minima of a given ω now correspond to different Hamiltonians, so the above "no crossing" rule is no longer valid. Similar consideration are also true in the case of self-consistent HFB treatment, as pointed out by Sorensen.[25]

The numerical results and how several minima of $\delta\langle H-\omega J_x\rangle = 0$ may occur by variation of ν will now be discussed. Our calculations indicate first that pairing collapse does not happen in rare-earth nuclei up to spin I~20. Thus, it is not a source of backbending in ^{162}Er. On the other hand, we observe the crossing of the ground band and the decoupled two-quasi-particle band in all four nuclei under study. We notice that in the present calculations the decoupled band crossing can occur in two ways.

It can either occur by increasing the angular velocity ω while keeping the pairing parameter ν fixed (cf. Fig. 7), or it can occur in the study of CAP effect where ν is varied while ω is kept fixed (cf. Fig. 12). As we have already discussed, the first type of crossing in ω-space with ν kept constant will not produce backbending, but the second type of crossing in ν-space with ω kept constant may produce two or more minima, thus making it possible for backbending to happen.

Until now the decoupled band crossing in the ν-space is quite smooth (cf. Fig. 12), and we always obtain one minimum in the variation of ν; thus backbending is not found. However, the way the decoupled band crosses depends strongly on the single-particle levels located near the chemical potential λ. It is at this point that the uncertainty sets in. Although the single-particle levels as a whole are well described by Nilsson model, the spacing between individual levels, nevertheless may be in error by several hundred keV. In the following we shall try to shift the single-particle levels to study the sensitivity of the backbending phenomenon.

In the case of ^{162}Er the neutron chemical potential λ_n is located between the i 13/2, 3/2 [651] state and the 5/2 [642] state. These states have energies of $6.344\hbar\omega_0$ and $6.457\hbar\omega_0$, respectively. It is not our intention here to search for better single-particle neutron levels. Instead the emphasis is to study their influence on the backbending. Therefore we arbitrarily shift the energy of the 3/2[651] state to three different values, namely $6.37\hbar\omega_0$, $6.40\hbar\omega_0$ and $6.42\hbar\omega_0$ (denoted as calculation B) and repeat the FBCS calculations. In the first case, backbending still does not happen; in the second case it occurs at

I = 6 and in the third case (calculation B) it occurs at I = 12, while experimentally backbending occurs at I = 16.

The reason that one obtains backbending in the third case is the following. First one observes that the band crossing in the ν-space is now sharper than the previous one in which the original Nilsson single-particle levels are used, see Fig. 12. One then finds that in the study of the CAP effect, the variation of $\delta\langle H-\omega J_x\rangle = 0$ with respect to the neutron pairing parameter ν_n has one minimum for $\omega<0.170$ MeV; it has two minima for $0.170 \leq \omega \leq 0.185$, and again it has only one minimum for $\omega >$ 0.185 MeV. The results are plotted in Fig. 13, the existence of two minima for a given value of ω in the above-mentioned region thus produces the backbending.

The nature of the solutions at these two minima are very different. In order to illustrate this, the vacuum amplitude of the N+ solution $a_0(N+)$ is plotted against ν_n at three values of ω in Fig. 14. For $\omega = 0.16$, there exists only one minimu at $\nu_n = 0.98$ with $a_0(N+) = 9.980$; thus the solution belongs to the ground band. For $\omega = 0.18$, there are two mimima, the first one is located at $\nu_n = 0.96$ with $a_0(N+) = 0.956$, while the second one is located at $\nu_n = 0.74$ with $a_0(N+) = 0.076$. Obviously, the first solution has the character of the ground band, while the second solution has the character of the decoupled band. Thus, two solutions of different nature coexist at $\omega = 0.18$ MeV. For $\omega = 0.20$ MeV, there exists again only one minimum at $\nu_n = 0.73$ with $a_0(N+) = 0.075$; thus, the solution belongs to the decoupled band.

By interpolating the solutions from $\omega = 0$ to $\omega = 0.185$ MeV of the upper branch ($\nu_n \gtrsim 0.90$) in Fig. 13, the states of spin I = 2, 4 can be obtained. On the other hand, the states of spin I = 12, 14, 16, 18 can

be obtained by interpolating the solutions from $\omega = 0.170$ to $\omega = 0.40$ of the lower branch ($\nu_n \lesssim 0.75$). However, we are unable to obtain the solutions of spin I = 6, 8, 10 by variation of $\delta\langle H-\omega J_x\rangle = 0$. In fact, they are obtained by variation of $\delta\langle H\rangle = 0$ with $\langle J_x\rangle = [I(I+1)]^{1/2}$. That is, the cranking equation is first solved on a two dimensional mesh of points (ν_i,ω_j). For each ν_i the results are interpolated to give the solution of a given spin I, and the minimum of $\delta\langle H\rangle = 0$ with variation of ν can then be searched. This method works very well in the backbending region, and both methods yield the same results for other spins. The present results resemble those of the HFB cranking model calculations of Banerjee et al.[2] They vary the set of V_k and find two minima of $\delta\langle H-\omega J_x\rangle = 0$ in the region of $0.2044 \lesssim \omega \lesssim 0.2099$, and they too are unable to obtain the solutions of I = 10, 12 by variation of $\delta\langle H-\omega J_x\rangle = 0$.

The calculation with the i13/2,3/2[651] single-particle energy shifted to $6.42\hbar\omega_0$ is denoted as calculation B; its energies are plotted in Fig. 15 together with the FBCS results calculated with the original Nilsson levels. One notices first that on the average the latter is better, but the former produce backbending while the latter does not. Second, in calculation B the enrgy interval $\Delta E(10 \to 8)$ is smaller than the $\Delta E(8 \to 6)$ by 3 keV which seems to be insignificant while the energy interval $\Delta E(12 \to 10)$ is smaller than the $\Delta E(10 \to 8)$ by 17 keV; thus, we consider the backbending occurs at spin I = 12. Experimentally the backbending occurs at I = 16. In order to understand the differnence we observe that the two quasi-particles in the N+ solution at spin I = 12 are already decoupled. In fact the value of $\langle J_x\rangle$ of the N+ solution alone increases from 9.2 at I = 12 ($\omega = 0.19$) to 10.3 at I = 18 ($\omega = 0.40$). On the other hand,

the $\langle J_x \rangle$ of the N- solution at I = 12 is 1.8 and that of the proton solution is 1.5. This suggests that in order to raise the value of spin at which the backbending occurs one probalby has to increase the contribution to the angular momentum by the N-, P+ and P- solutions, which represent the rotating core.

We now compare the wave functions of the N+ solutions to those of the neutron i13/2 solutions of Stephens and Simon.[7] Only the six largest amplitudes of the states at the band-crossing region are listed in Table II which are the states of spin I = 10, 12 in our case and the states of I = 16, 18 in theirs. For comparison purpose our listed wave functions are those without CAP effect. It is interesting to see that the two sets of wave functions are quite similar to each other.

The above results seem to indicate that the backbending behavior is very sensitive to the exact spacing of the single-particle levels near the chemical potential λ. This is understandable because the present calculations show that the decoupled band crossing occurs in the N+ solutions for all rare-earth nuclei below spin 20, but there is a strong influence of the local single-particle levels near λ determining how sharply the corssing occurs, causing some nuclei to backbend while near neighbors do not. However, the present calculated result of backbending probably is too sensitive to the single-particle level spacing, perhaps due to the spreading in $\langle J_x \rangle$ at the band-crossing region. Cranking calculations with angular momentum projection will certainly provide deeper insight into this problem.

5.5 The excited solutions

So far we have focused our attention only on the lowest solution,

which corresponds to the yrast band. The diagonalization, unlike variation, also gives many other solutions at higher energies. Since the total wave function is the product of the P+, P-, N+ and N- solutions, for rare-earth nuclei the lowest solution (n = 1) is

$$|n = 1\rangle = |P+, n = 1\rangle\, |P-, n = 1\rangle\, |N-, n = 1\rangle\, |N+, n = 1\rangle$$

while the second lowest solution (n = 2) is

$$|n = 2\rangle = |P+, n = 1\rangle\, |P-, n = 1\rangle\, |N-, n = 1\rangle\, |N+, n = 2\rangle .$$

We have already mentioned before that the lowest N+ solution crosses the second lowest N+ solution at high spin, see Fig. 7. Therefore it is of interest to know whether the second solution after crossing will form a second branch of the ground band. In Fig. 16, the energies of the two lowest solutions of the FBCS calculation with CAP effect included are plotted as function of spin I for ^{174}Hf. The lower curve represents the n = 1 solution while the upper curve represents the n = 2 solution. Some of the corresponding ω values are also indicated along the curve. The cusp of the upper curve where the total spin decreases with increasing value of ω results from the band crossing. This is because the vacuum amplitude of the second N+ solution increases with ω due to crossing (see the graph at the upper corner of Fig. 16); as a result, the angular momentum of the N+ solution decreases with increasing ω although the angular momenta of the P+, P- and N- solutions, which represent the core, continue to increase. Figure 16 seems to indicate that it is possible that a second branch of the ground band may appear at high spin. However, the above discussion is only preliminary, since our result of the excited solution resembles the HFB calculation of Hamamoto[24], who showed that the excited solution contains large spreading in $\langle J_x \rangle$.

Therefore care must be taken in interpreting the excited state solutions. We have not felt it justified to calculate B(E2) transition rate values between bands because of non-orthogonality uncertainties. That is, our ground and excited solutions are orthogonal at fixed angular velocity ω, but in general these solutions correspond to different angular momentum I. Hench at fixed I and different ω the solutions may depart from orthogonality. Any detailed interpretation of the multiple-valued solutions at fixed I in the I~12 cusp region of Fig. 16 must also take the non-orthogonality problem into account.

6. Conclusions

The high-spin rotational states of ^{162}Er, ^{168}Yb, ^{174}Hf, and ^{238}U were calculated microscopically by diagonalizing the cranking model using both BCS and fully particle-number-projection wave functions. The results show that the fixed-particle-number correction does not increase appreciably as the spin goes up; thus, the BCS method can still be applied to high-spin states without serious error. We have studied three sources that cause the moment-of-inertia $\mathcal{J}$ to increase, the CAP effect, the higher-order cranking and the decoupled band crossing with the deformation kept fixed. The first two factors both contribute significantly to the slow increase of $\mathcal{J}$ at low spin. The third one is mainly responsible for the rapid increase of $\mathcal{J}$ at high spin. We do not find pairing collapse; in fact substantial proton and neutron pairing still remain up to spin I~20.

In the present calculations, the self-consistent treatment of the pairing effect is vital in order to obtain backbending behavior, which

also depends very strongly on the two high-j low-Ω quasi-particles being near to the chemical potential. These results are affected to some extent by the undetermined spreading in $\langle J_x \rangle$ of the cranking solution at the band-crossing region. A deeper understanding of backbending behavior thus calls for a more careful study of the $\langle J_x \rangle$ spreading problem.

The problem of nuclear rotational band theory and backbending must be regarded as still open, despite all the cranking model and HFB studies to date. We believe that our demonstration in Sec. 5.4 of the great sensitivity of backbending to shift of just one orbital energy near the chemical potential underscores the difficulty of exact matching of theory and experiment. It is often not clear in HFB calculations just how well the orbital energies near the chemical potential match experimental observations from the band head energies in neighboring odd-mass nuclei. Our calculation, though lacking the number of variational parameters of some HFB studies and lacking self-consistency in the imposed average field, has the advantage of being closely tied to the sophisticated 1969 version of the Nilsson model, with potential parameters and pairing constants fine-tuned to reproduce well the experimental level ordering, the occurrence of subshells, and the odd-even mass differences.

One of the important next steps, though difficult, will be for calculations to incorporate a more realistic Hamiltonian than pairing plus quadrupole-quadrupole or surface delta interactions. Even for the simpler cases of spherical near-closed-shell nuclei the effective residual shell model interaction question is not resolved, despite advances through Kuo-Brown renormalization, use of density-dependent, velocity-dependent

interactions, Skyrme forces, etc. We pointed out some time ago that the constant pairing matrix element approximation systematically deviates from results of a delta force or finite-range Gaussian force.[27] Namely, the more realistic forces give diagonal pairing matrix elements considerably larger than off-diagonal. Thus, there is actually less pairing configuration mixing than is given in the ordinary constant pairing treatments. See for example the recent work of Chasman on deformed nuclei using a density-dependent delta interaction.[28] This interaction would seem promising for future calculations of the nuclear rotational state properties. Of course, refined treatments should take into account the full H_{22} interaction between quasi-particles. In view of the great complexity of the microscopic nuclear rotational theory it is encouraging that there is additional experimental information coming forth, as very heavy ion beams are used to measure E2 matrix elements between high-lying rotational states of ground and crossing bands in the backbending region.

Acknowledgements

We are grateful to Drs. T. Kishimoto and R. A. Sorensen for helpful discussions; and to Dr. R. Simon for useful discussions and for providing his unpublished detailed wave functions from band-mixing calculations. We also thank Drs. M. Sano (Muraoka) and K. Dietrich for their interest and comments on this work.

Appendix

A. Derivation of equation (3.5):

We want to prove first the following auxiliary formula

$$\gamma^n = \delta_{nN} \prod_{i=\nu_1 \cdots \nu_N} \frac{U_i^2 + \gamma V_i^2}{V_i^2} + (-1)^n \sum_{i=\nu_1 \cdots \nu_N} V_i^{2(N-n-1)} U_i^{2n} \prod_{\substack{k=\nu_1 \cdots \nu_N \\ \neq i}} \frac{U_k^2 + \gamma V_k^2}{V_i^2 - V_k^2} \qquad N \geq n \quad \text{(A1)}$$

a. n = 0:

It is easy to show that eq. (A1) with n = 0 is correct for N = 1, 2, 3. Now if (A1) holds for n = 0 and N = M + 1, then consider the identity

$$1 = \frac{V_s^2}{V_s^2 - V_t^2}(U_t^2 + \gamma V_t^2) + \frac{V_t^2}{V_t^2 - V_s^2}(U_s^2 + \gamma V_s^2) . \quad \text{(A2)}$$

Multiplying the first and the second term in the right-hand side separately by (A1) with n = 0, N = M + 1,

$$1 = \frac{V_s^2}{V_s^2 - V_t^2}(U_t^2 + \gamma V_t^2) \sum_{i=\nu_1 \cdots \nu_M, s} V_i^{2M} \prod_{k=\nu_1 \cdots \nu_M, s} \frac{U_k^2 + \gamma V_k^2}{V_i^2 - V_k^2}$$

$$+ \frac{V_t^2}{V_t^2 - V_s^2}(U_t^2 + \gamma V_s^2) \sum_{i=\nu_1 \cdots \nu_M, t} V_i^{2M} \prod_{\substack{k=\nu_1 \cdots \nu_M, t \\ \neq i}} \frac{U_k^2 + \gamma V_k^2}{V_i^2 - V_k^2} ,$$

then it is straighforward to show that (A1) also holds for n = 0 and N = M + 2. Thus eq. (A1) is correct for n = 0 and any $N \geq 1$, namely

$$1 = \sum_{i=\nu_1 \cdots \nu_N} V_i^{2(N-1)} \prod_{\substack{k=\nu_1 \cdots \nu_N \\ \neq i}} \frac{U_k^2 + \gamma V_k^2}{V_i^2 - V_k^2} \qquad N \geq 1 \quad \text{(A3)}$$

b. n = 1:

Consider the identity

$$\zeta = \frac{U_*^2 + \zeta V_*^2}{V_*^2} - \frac{U_*^2}{V_*^2} \quad . \tag{A4}$$

It is obvious that (A1) reduces to (A4) for N = n = 1. For N≥2, we multiply separately the first and the second term on the right-hand side by (A3), but one with N = M and the other with N = M + 1. Then it is easy to show that eq. (A1) holds for n = 1 and N≥2.

c. n = 2

Consider the identity

$$\zeta^2 = \frac{U_*^2 + \zeta V_*^2}{V_*^2}\,\zeta - \frac{U_*^2}{V_*^2}\,\zeta \quad . \tag{A5}$$

Replacing z in the first and the second term on the right-hand side spearately by (A1), but one with n = 1, N = M≥1 and the other with n = 1, N = M + 1, one can show that eq. (A1) is true for n = 2.

d. Arbitrary n:

We have now shown that (A1) is correct for n = 0, 1, 2. If (A1) holds for n = m, then consider the identity

$$\zeta^{m+1} = \frac{U_*^2 + \zeta V_*^2}{V_*^2}\,\zeta^m - \frac{U_*^2}{V_*^2}\,\zeta^m \quad . \tag{A6}$$

By applying a similar method to that described above, one can show that (A1) is also true for n = m + 1. Therefore eq. (A1) holds for any value of n.

One can now substitute z^n inside the integral of eq. (3.4) by (A1), this immediately yields eq. (3.5).

B. Matrix elements used in the FBCS calculations:

We list below some of the Hamiltonian and J_x matrix elements using FBCS wave functions (3.1)-(3.3).

$$\langle \phi_0 | H | \phi_0 \rangle = \frac{1}{R_0^0} \sum_{k>0} 2\varepsilon_k V_k^2 R_1'(k) - \frac{1}{R_0^0} G \sum_{k>0} V_k^2 R_1'(k) - \frac{1}{R_0^0} G \sum_{\substack{p,q>0 \\ p\neq q}} U_p V_p U_q V_q R_1^2(p,q) \tag{B1}$$

$$\langle \phi_{k\bar{k}} | H | \phi_{k\bar{k}} \rangle = \frac{1}{R_1'(k) + R_0'(k) - R_0^0} \times \left[\begin{array}{l} (2\varepsilon_k - G) U_k^2 R_1'(k) + 2G U_k V_k \sum_{\substack{p>0 \\ \neq k}} U_p V_p R_1^2(k,p) \\ + \sum_{\substack{p>0 \\ \neq k}} (2\varepsilon_p - G) V_p^2 (U_k^2 R_2^2(k,p) + V_k^2 R_1^2(k,p)) \\ - G \sum_{\substack{p,q>0 \\ p\neq q\neq k}} U_p V_p U_q V_q (U_k^2 R_2^3(k,p,q) \\ \qquad + V_k^2 R_1^3(k,p,q)) \end{array} \right]$$

$$\langle \phi_{kl} | H | \phi_{kl} \rangle = \frac{1}{R_1^2(k,l)} \left[\begin{array}{l} (\varepsilon_k + \varepsilon_l) R_1^2(k,l) \\ + \sum_{\substack{p>0 \\ \neq k,l}} (2\varepsilon_p - G) V_p^2 R_2^3(k,l,p) \\ - G \sum_{\substack{p,q>0 \\ p\neq q\neq k\neq l}} U_p V_p U_q V_q R_2^4(k,l,p,q) \end{array} \right]$$

$$\langle \phi_0 | J_x | \phi_{pq} \rangle = -\left[\frac{R_1^2(p,q)}{R_0^0}\right]^{\frac{1}{2}} \langle p | j_x | \bar{q} \rangle (U_p V_q - V_p U_q)$$

$$\langle \phi_{k-k} | J_x | \phi_{pq} \rangle = \left[\frac{R_1^2(p,q)}{R_1^1(k) + R_0^1(k) - R_0^0}\right]^{\frac{1}{2}}$$

$$\times \langle p | j_x | -q \rangle (U_p U_q + V_p V_q)(\delta_{kp} - \delta_{kq} - \delta_{-kp} + \delta_{-kq})$$

$$\langle \phi_{kl} | J_x | \phi_{pq} \rangle = \frac{1}{[R_1^2(k,l)\, R_1^2(p,q)]^{\frac{1}{2}}}$$

$$\times \left\{ \begin{array}{l} \delta_{kp} \langle l | j_x | q \rangle [U_l U_q R_1^3(k,l,q) + V_l V_q R_2^3(k,l,q)] \\ -\delta_{kq} \langle l | j_x | p \rangle [U_l U_p R_1^3(k,l,p) + V_l V_p R_2^3(k,l,p)] \\ -\delta_{lp} \langle k | j_x | q \rangle [U_k U_q R_1^3(k,l,q) + V_k V_q R_2^3(k,l,q)] \\ +\delta_{lq} \langle k | j_x | p \rangle [U_k U_p R_1^3(k,l,p) + V_k V_p R_2^3(k,l,p)] \end{array} \right\}$$

It is then simple to calculate the matrix elements in the symmetric representation $\|+\}$, see eqn. (4.3).

References

* Work supported in part by the National Science Foundation and by the U. S. Energy Research and Development Administration

[1]See the review articles: R. A. Sorensen, Rev. Mod. Phys. 45, 353 (1973); F.S. Stephens, Rev. Mod. Phys. 47, 43 (1975); G. Scharff-Goldhaber, C. Dover, and A. L. Goodman, Ann. Rev. Nucl. Sci. 26 and references therein.

[2]B. Banerjee, H. J. Mang, and P. Ring, Nucl. Phys. A215, 366 (1973).

[3]P. C. Bhargava and D. J. Thouless, Nucl. Phys. A215, 515 (1973).

[4]A. L. Goodman, Nucl. Phys. A265, 113 (1976).

[5]A. Faessler, K. R. Sandhya Devi, F. Grümmer, K. W. Schmid, and R. R. Hilton, Nucl. Phys. A256, 106 (1976).

[6]K. W. Schmid, H. Müther, K. Goeke, and A. Faessler, Phys. Lett. 63B, 399 (1976).

[7]F. S. Stephens and R. S. Simon, Nucl. Phys. A183, 257 (1972).

[8]B. R. Mottelson and J. G. Valatin, Phys. Rev. Lett. 5, 511 (1960).

[9]S. G. Nilsson, C. F. Tsang, A. Sobiczewski, Z. Szymanski, S. Wycech, C. Gustafson, I. L. Lamm, P. Möller, and B. Nilsson, Nucl. Phys. A131, 1 (1969).

[10]S. G. Nilsson and O. Prior, K. Dan. Vidensk. Selsk. Mat.-Fys. Medd. 32, No. 16 (1961).

[11]E. R. Marshalek, Phys. Rev. 158, 993 (1967); C. W. Ma and C. F. Tsang, Phys. Rev. C 11, 213 (1975).

[12]M. Rich, Nucl. Phys. A90, 407 (1967).

[13]H. R. Dalafi, B. Banerjee, H. J. Mang, and P. Ring, Phys. Lett. 44B, 327 (1973).

[14]A. Faessler, F. Grümmer, L. Lin, and J. Urbano, Phys. Lett. 48B, 87 (1974).

[15]R. A. Sorensen, Phys. Lett. 38B, 376 (1972).

[16]A. Faessler, "Backbending: Coriolis Antipairing or Rotational Alignment? Very high spin (up to 80ħ) States," invited paper, Symposium on Nuclear Structure, September 1-6, 1975, Balatonfüred, Hungary.

[17]K. Dietrich, H. J. Mang, and J. H. Pradal, Phys. Rev. 135, B22 (1964).

[18]A. L. Goodman, Nucl. Phys. A230, 466 (1974).

[19]K. Kumar and M. Baranger, Nucl. Phys. A92, 608 (1967).

[20]R. O. Sayer, J. S. Smith, III, and W. T. Milner, Atomic Data Nucl. Data Tables 15, 85 (1975).

[21]G. Gross, J. de Boer, R. M. Diamond, F. S. Stephens, and P. Tjøm, Phys. Rev. Lett. 35, 565 (1975).

[22]H. Bohn, T. V. Egidy, Th. Faestermann, F. V. Feilitzsch, P. Kienle, H. J. Körner and J. P. Schiffer, "High Spin States in ^{174}Hf", Proceedings of the INS International Symposium on Collectivity of Medium and Heavy Nuclei; September 23-25, 1975, Tokyo, Japan.

[23]O. Prior, F. Boehm, and S. G. Nilsson, Nucl. Phys. A110, 257 (1968).

[24]I. Hamamoto, Nucl. Phys. A271, 15 (1976).

[25]R. A. Sorensen, "Treatment of the pairing force by cranked HFB, a model of backbending", to be published.

[26]S. Y. Chu, E. R. Marshalek, P. Ring, J. Krumlinde, and J. O. Rasmussen, Phys. Rev. C 12, 1017 (1975).

[27]J. O. Rasmussen and C. W. Ma, Z. fur Physik 202, 182 (1967).

[28]R. R. Chasman, "Density dependent delta interactions and actinide pairing matrix elements" (to be published).

Table I. The quadrupole and hexadecapole deformation parameters ε_2 and ε_4 are taken from Ref. 9. The pairing parameters $\nu_{0\tau}$(BCS) and $\nu_{0\tau}$(FBCS) in MeV are calculated with pairing strength as given in Eqs. (4.1) and (4.4) where τ = proton or neutron.

Nucleus	ε_2	ε_4	ν_{0p}(BCS)	ν_{0p}(FBCS)	ν_{0n}(BCS)	ν_{0n}(FBCS)
^{162}Er	0.242	-0.007	0.935	1.015	0.915	0.975
^{168}Yb	0.255	0.014	0.900	0.990	0.815	0.830
^{174}Hf	0.258	0.034	0.860	0.910	0.765	0.810
^{238}U	0.205	-0.038	0.760	0.830	0.610	0.630

Table II. Comparison of the wave functions of the N+ solution of calculation B with those of the neuton i 13/2 solutions of Stephens and Simon (SS)[7]. Only the six largest amplitudes of the states at the band crossing region are listed. (Ω_i,Ω_j) denotes the I_z components of the two quasiparticles in the SS solutions

(Ω_i,Ω_j)	$\lvert\tilde{0}\rangle$	$(\frac{3}{2},-\frac{3}{2})$	$(\frac{5}{2},-\frac{3}{2})$	$(\frac{5}{2},-\frac{1}{2})$	$(\frac{7}{2},-\frac{5}{2})$	$(\frac{5}{2},\frac{1}{2})$
SS, I = 16	0.730	0.225	0.469	0.265	-0.178	0.152
Calc. B, I = 10	0.581	0.309	0.448	0.202	0.000	0.086
(Ω_i,Ω_j)	$\lvert\tilde{0}\rangle$	$(\frac{3}{2},-\frac{3}{2})$	$(\frac{5}{2},-\frac{5}{2})$	$(\frac{3}{2},-\frac{1}{2})$	$(\frac{5}{2},-\frac{3}{2})$	$(\frac{5}{2},-\frac{1}{2})$
SS, I = 18	0.329	0.325	0.219	0.289	0.498	0.389
Calc. B, I = 12	0.343	0.361	0.367	0.251	0.550	0.241

FIGURE CAPTIONS

Fig. 1 Energy E versus spin I(I+1) for ^{162}Er. The dashed curve represents the BCS calculation without Coriolis-antipairing effect, the dotted curve represents the same calculation with CAP effect, the solid curve is the fixed-particle-number-projection (FBCS) calculation also with CAP effect, and the dash-dot curve is the regular cranking result. The experimental data are indicated by dots.

Fig. 2 Energy E versus spin I(I+1) for ^{168}Yb, see Fig. 1 for detailed explanation.

Fig. 3 Energy E versus spin I(I+1) for ^{174}Hf, see Fig. 1 for detailed explanation.

Fig. 4 Energy E. versus spin I(I+1) for ^{238}U, see Fig. 1 for detailed explanation.

Fig. 5 The vacuum amplitude $a_o(\tau)$ in eq. (2.9) versus spin I, where τ(= P+, P-, N+ and N-) represents the proton and neutron solution with positive and negative parity, respectively.

Fig. 6 The contributions to $\langle J_x \rangle$ by the P+, P-, N+, and N- solutions are plotted as functions of spin I.

Fig. 7 The vacuum amplitudes a_0 of the lowest solution n = 1 and the second lowest solution n = 2 are plotted as functions of angular velocity ω, note the crossing of the two solutions.

Fig. 8 The ratio of the moment-of-inertia obtained by diagonalization to that obtained by second-order perturbation is plotted as a function of spin

Fig. 9 The collective gyromagnetic ratio g_R versus spin I.

Fig. 10 Coriolis-antipairing effect: the pairing parameters ν_p and ν_n are plotted as functions of spin I. The dotted curve represents the BCS results while the solid curve represents the FBCS results.

Fig. 11 The fractional increment of the moment-of-inertia $(\mathcal{J}_1 - \mathcal{J}_2)/\mathcal{J}_2$ versus spin I. The dotted curve represents calculations without CAP effect while the solid curve represents those with CAP effect.

Fig. 12 The vacuum amplitude a_0 of the N+ solution of ^{162}Er versus the pairing parameter ν_n for fixed angular velocity ω. The lower graph corresponds to calculations using the 1969 Nilsson single particle levels[9] while the upper graph represents calculations in which the neutron level 3/2 [651] is shifted.

Fig. 13 The neutron pairing parameter ν_n of ^{162}Er is plotted as a function of angular velocity ω for calculation B. Note the existence of two solutions in the region $0.170 \leq \omega \leq 0.185$.

Fig. 14 The vacuum amplitude a_0 of the N+ solutions of ^{162}Er versus the pairing parameter ν_n at three different values of ω. The dot denotes the solution which minimizes $\langle H - \omega J_x \rangle$.

Fig. 15 Comparison between the experimental and calculated rotational energies of ^{162}Er. The second column represents calculations in which the neutron level 3/2[651] is shifted while the third column represents calculations using the 1969 Nilsson energy levels[9]. The numbers between levels are their energy differences in keV. The symbol * has been used to indicate a backbending transition.

Fig. 16 Energy E versus spin I for ^{162}Er. The lower curve represents the lowest solution (n = 1) while the upper curve represents the second lowest solution (n = 2). The vacuum amplitudes a_0 of the two solutions are plotted as functions of angular velocity ω in the upper corner.

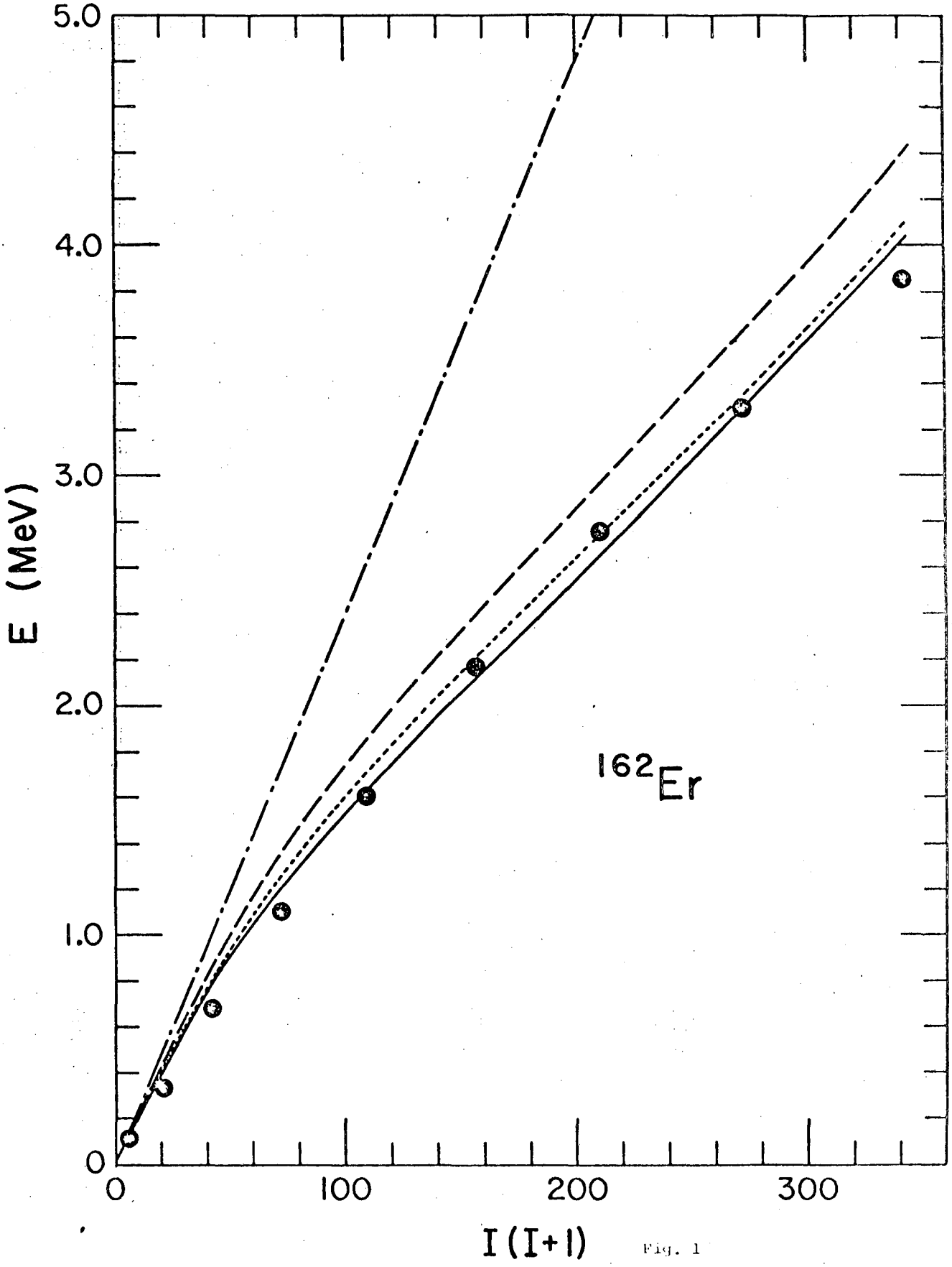

Fig. 1

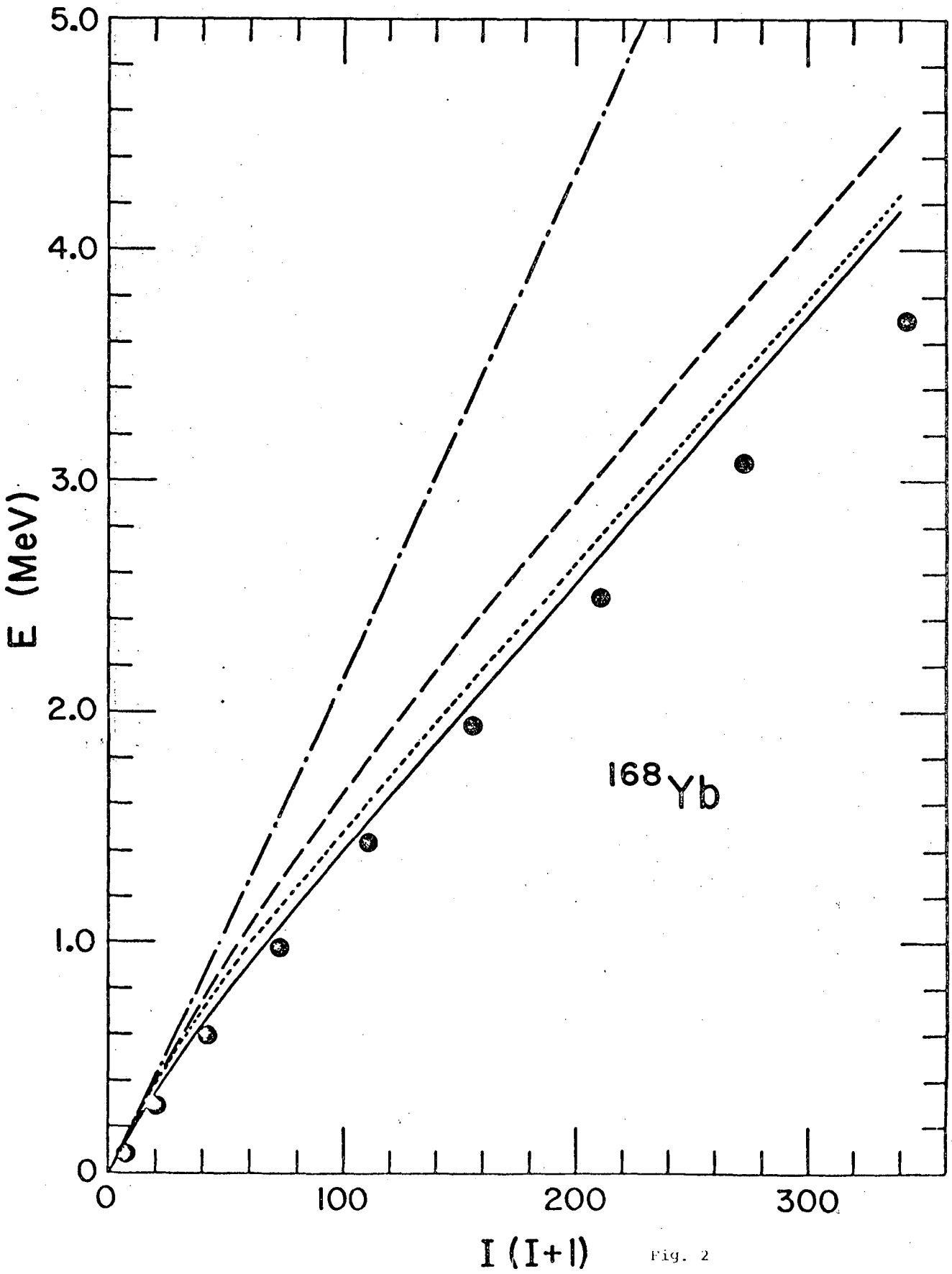

Fig. 2

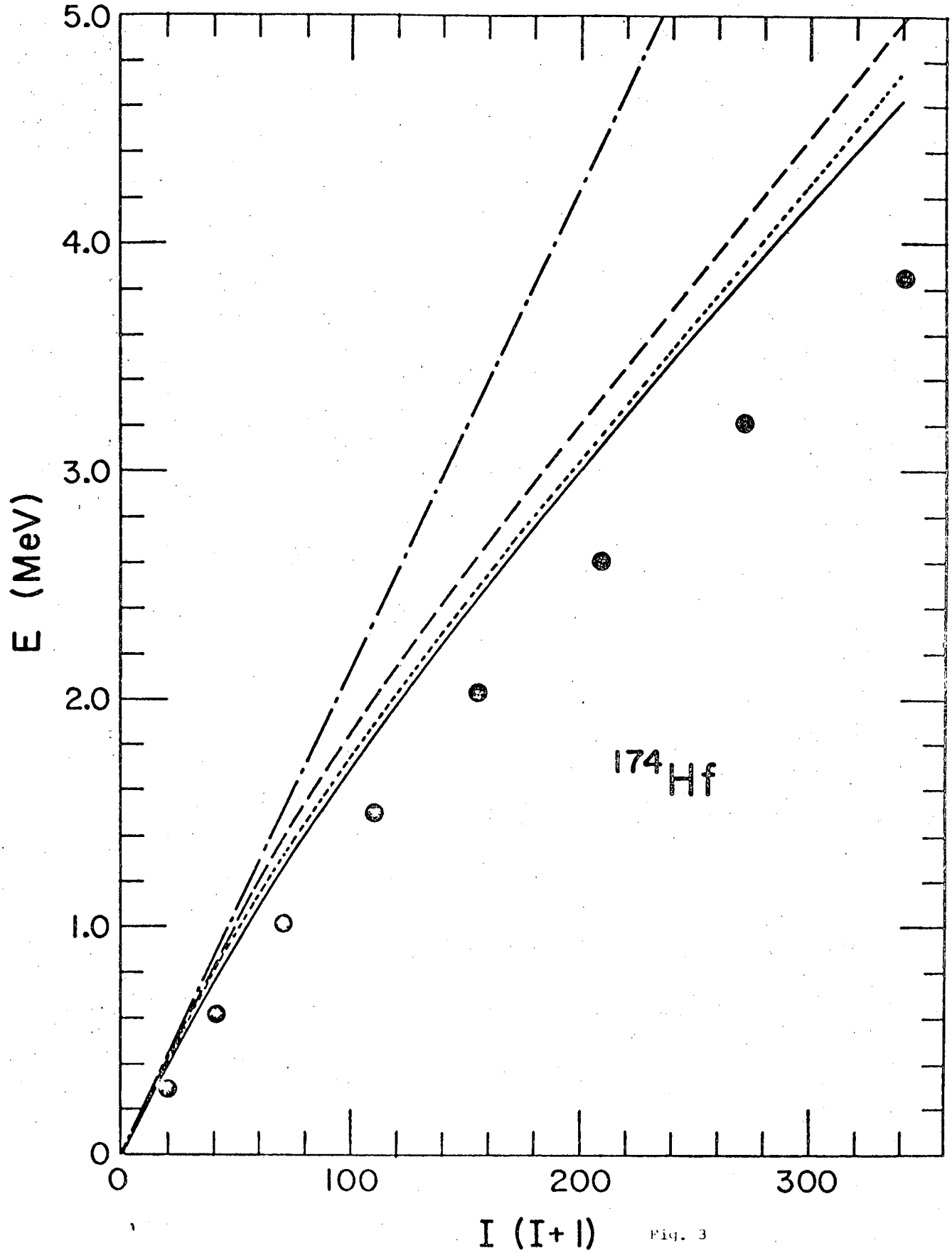

Fig. 3

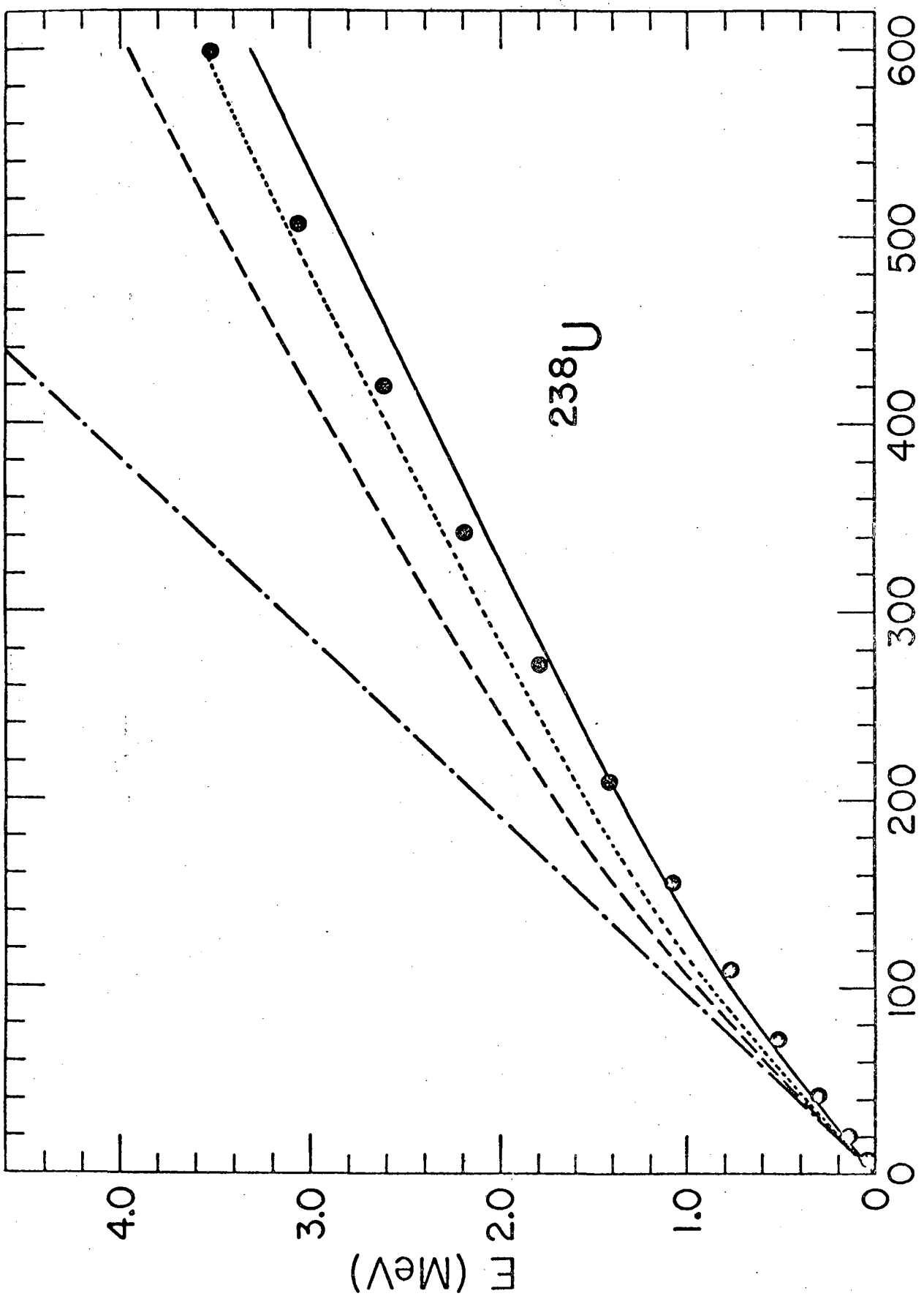

Fig. 4

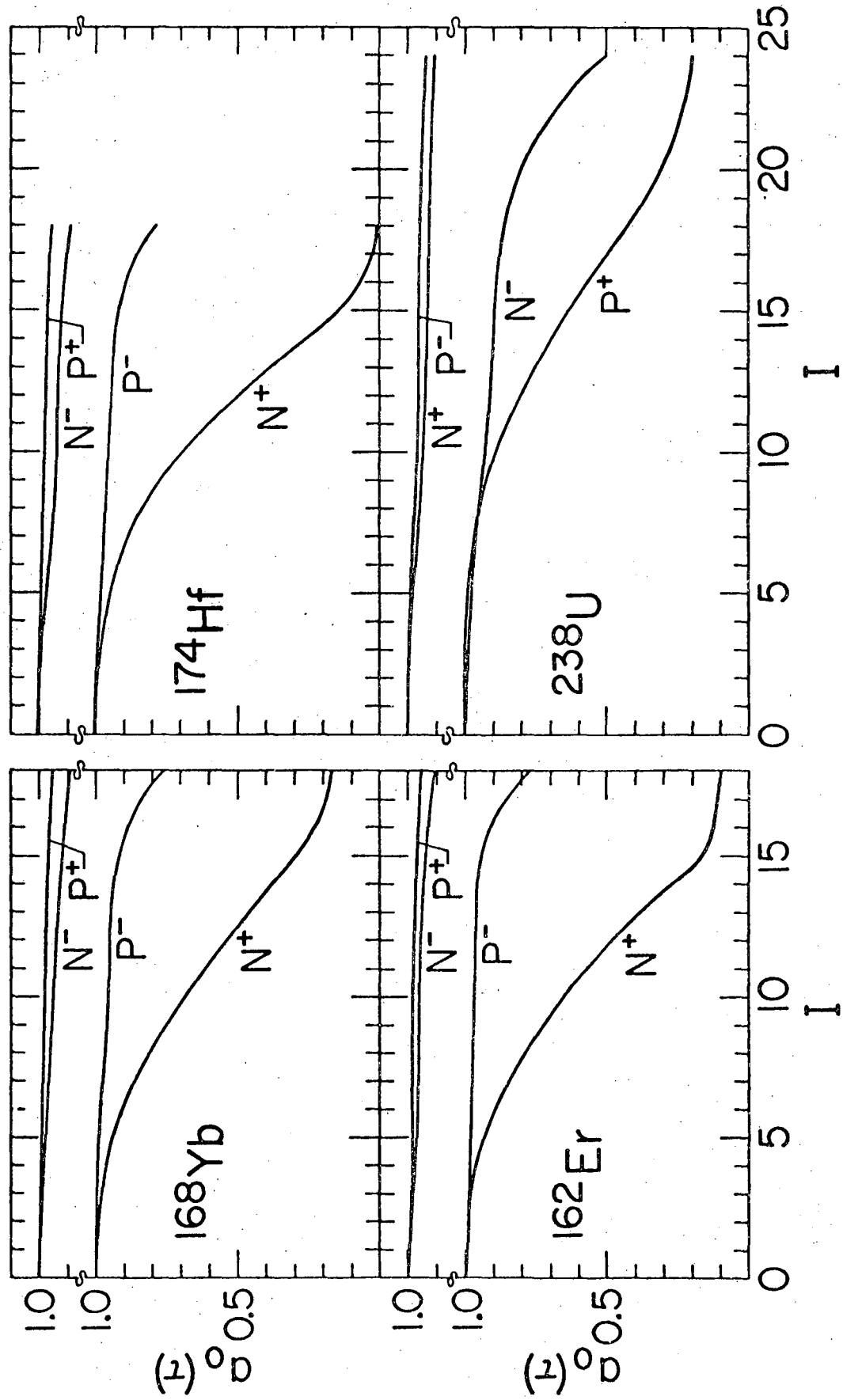

Fig. 5

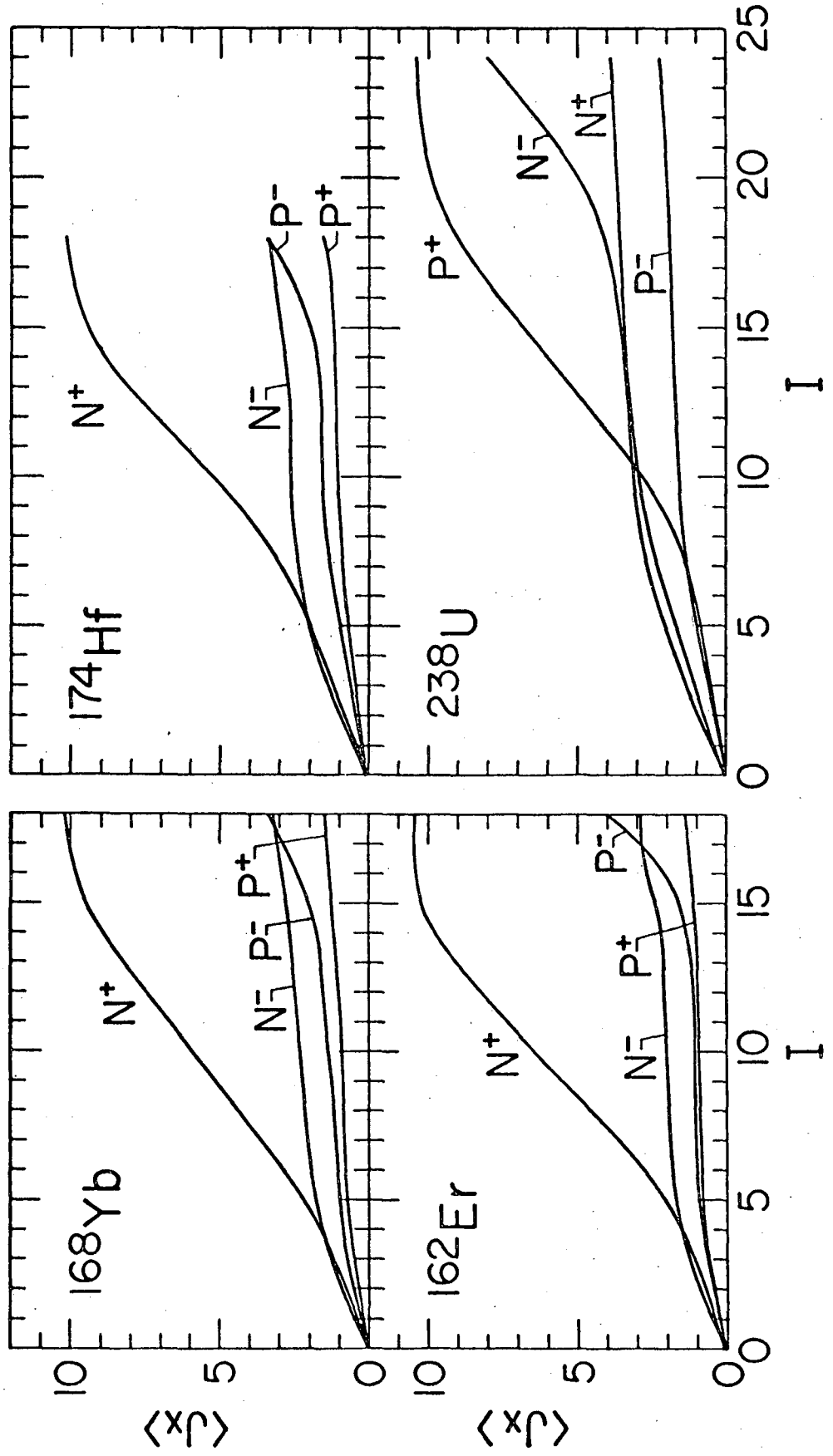

Fig. 6

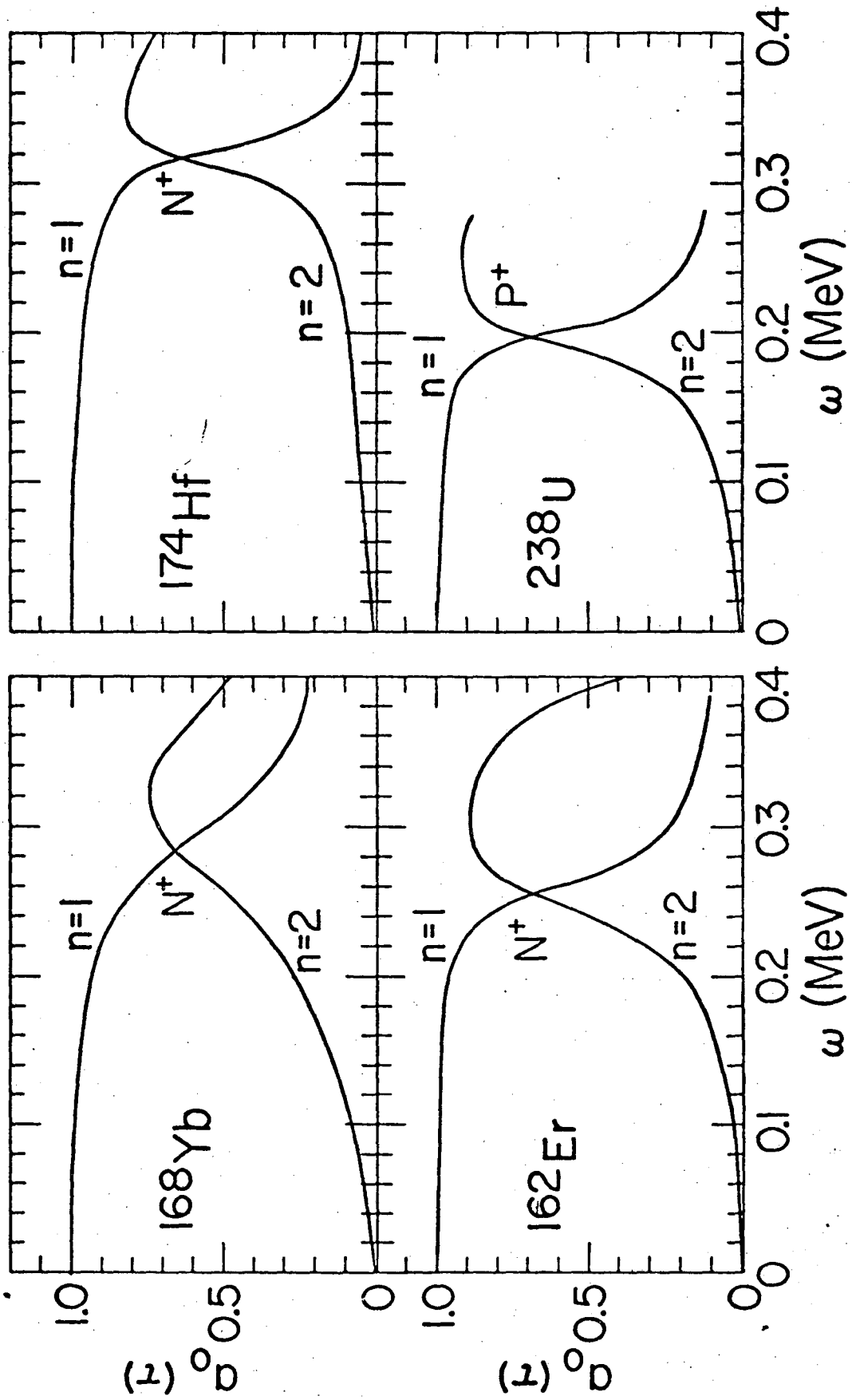

Fig. 7

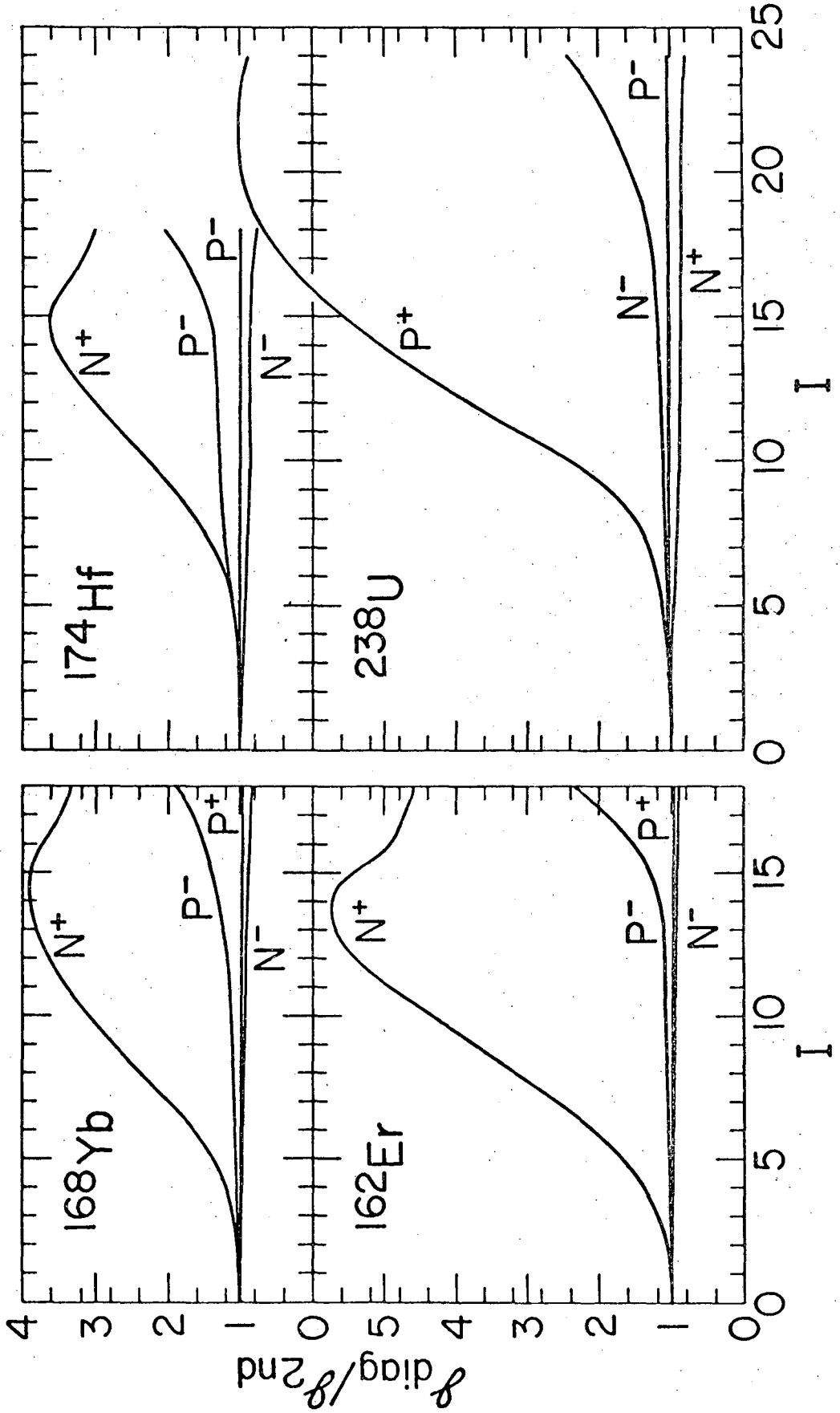

Fig. 8

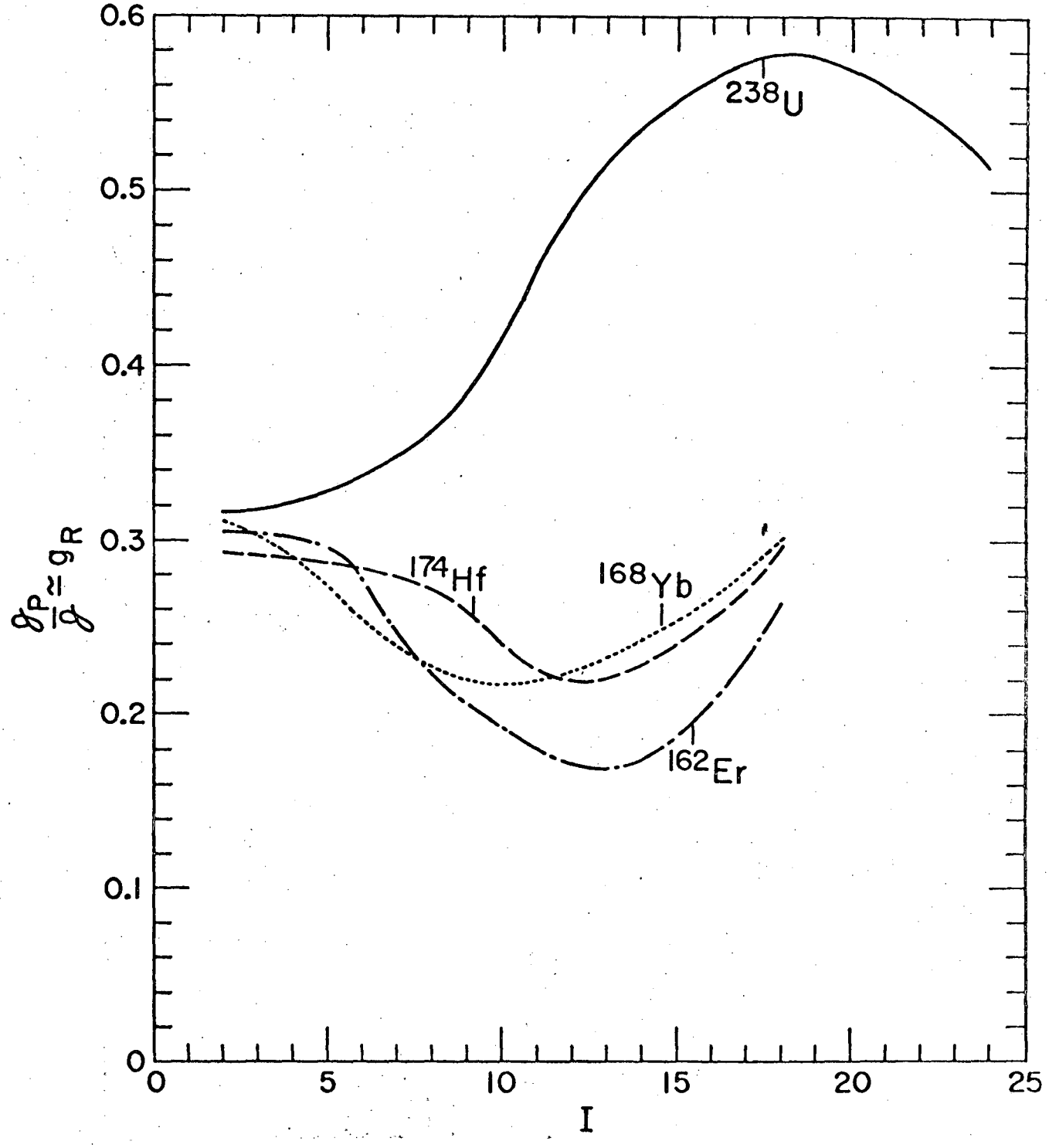

Fig. 9

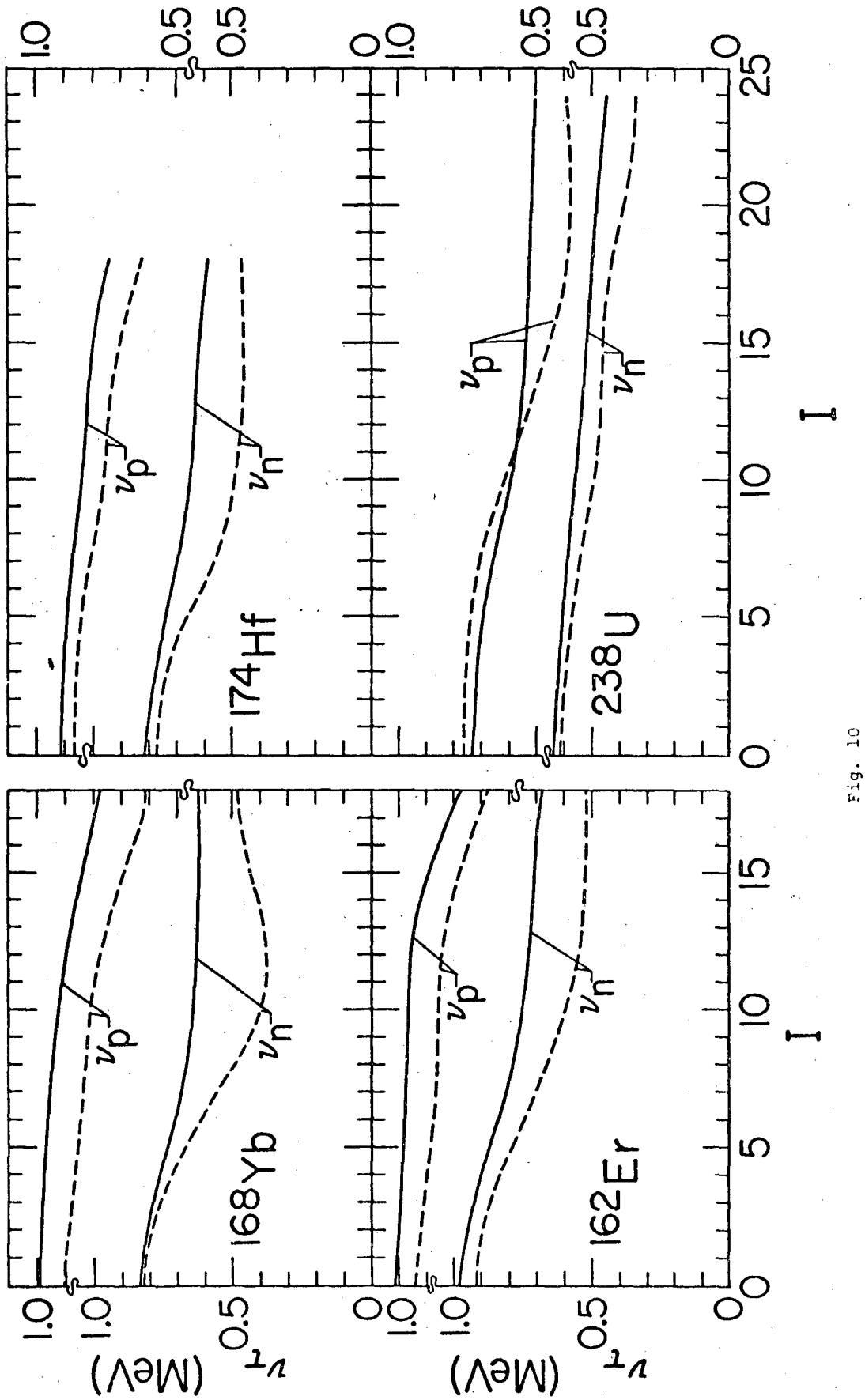

Fig. 10

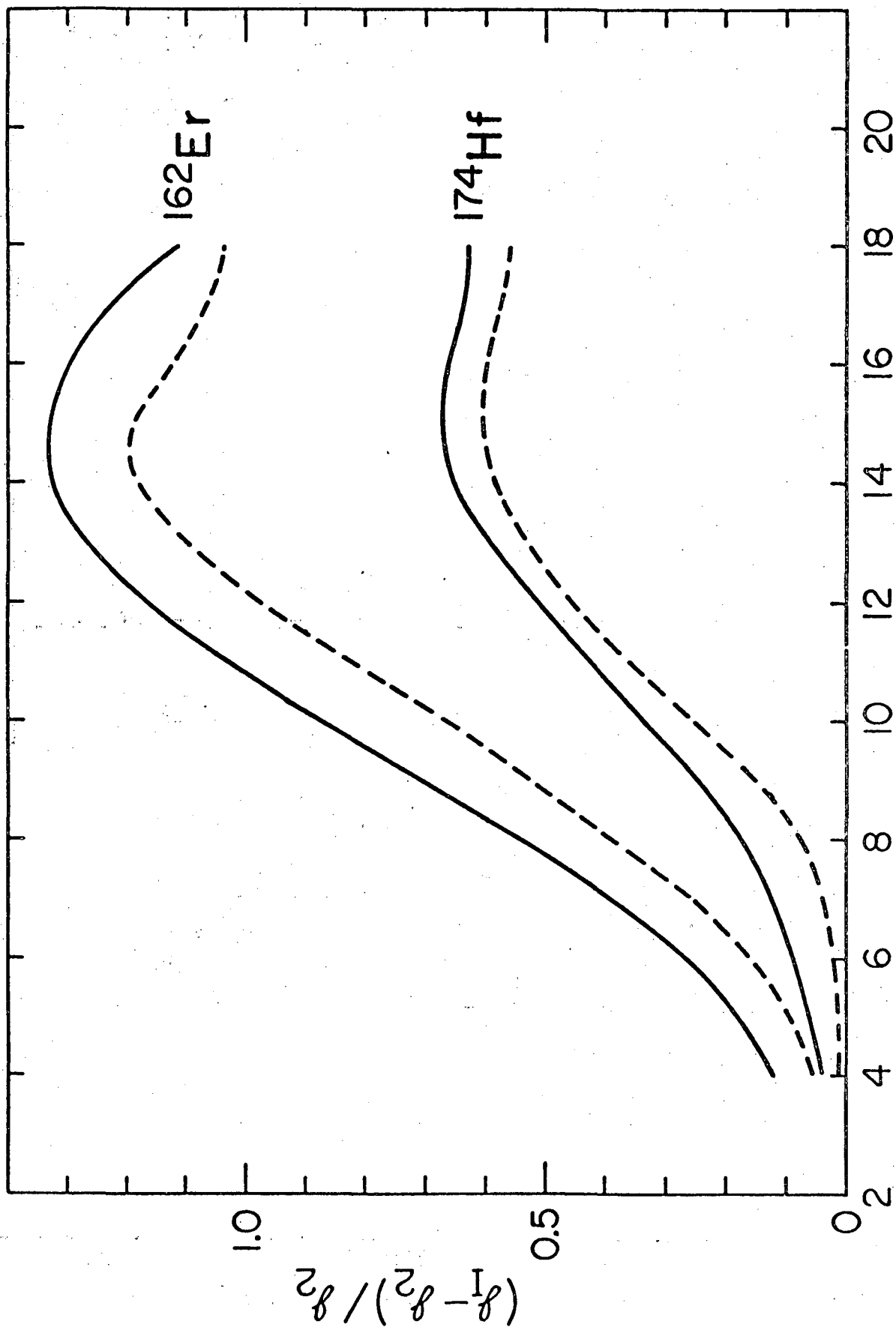

Fig. 11

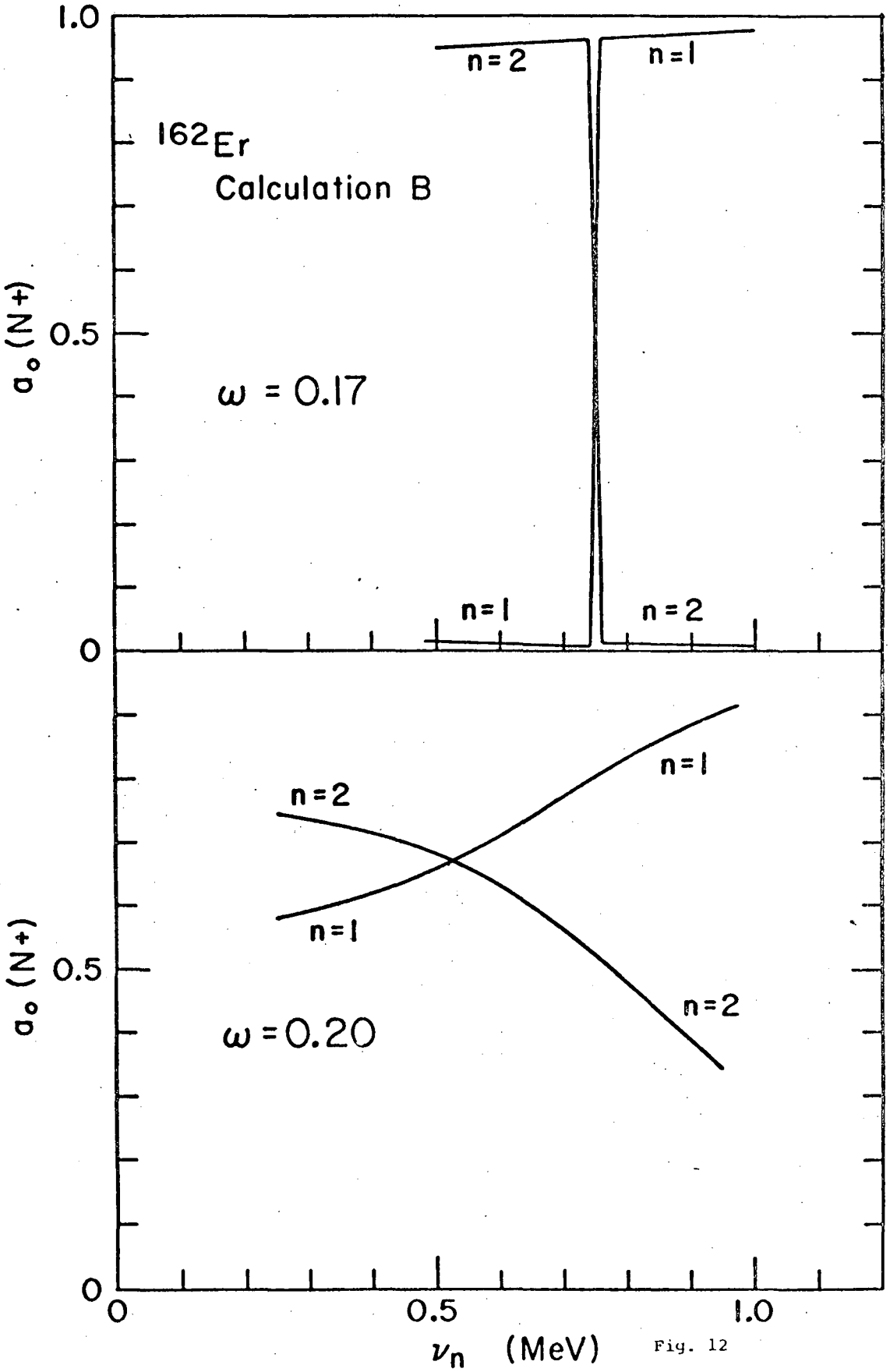
1.0
0.5
0
σ_o (N+)
^{162}Er
Calculation B
ω = 0.17
n=2
n=1
n=1
n=2
ω = 0.20
n=2
n=1
n=1
n=2
0
0.5
1.0
ν_n (MeV)

Fig. 12

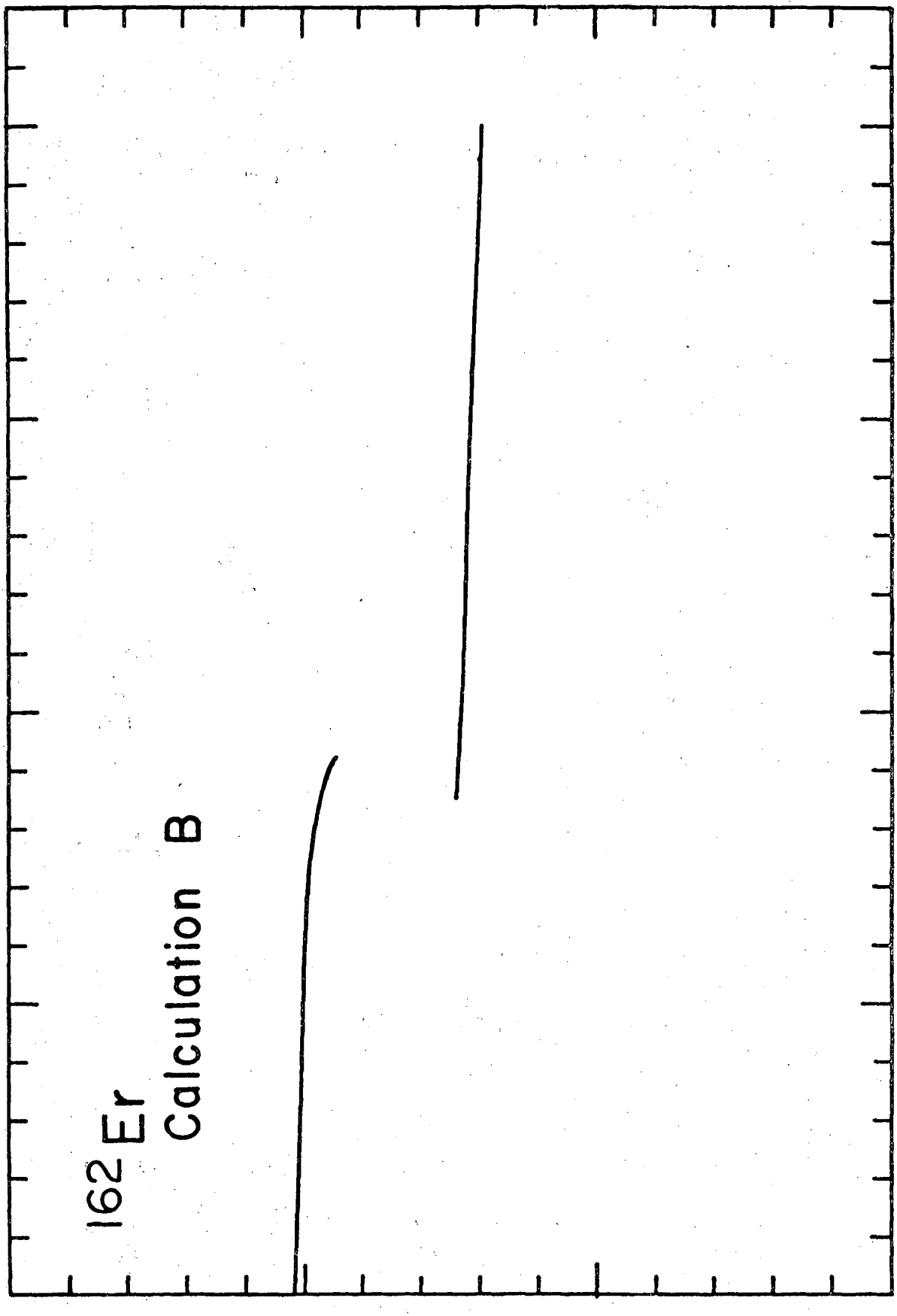

Fig. 13

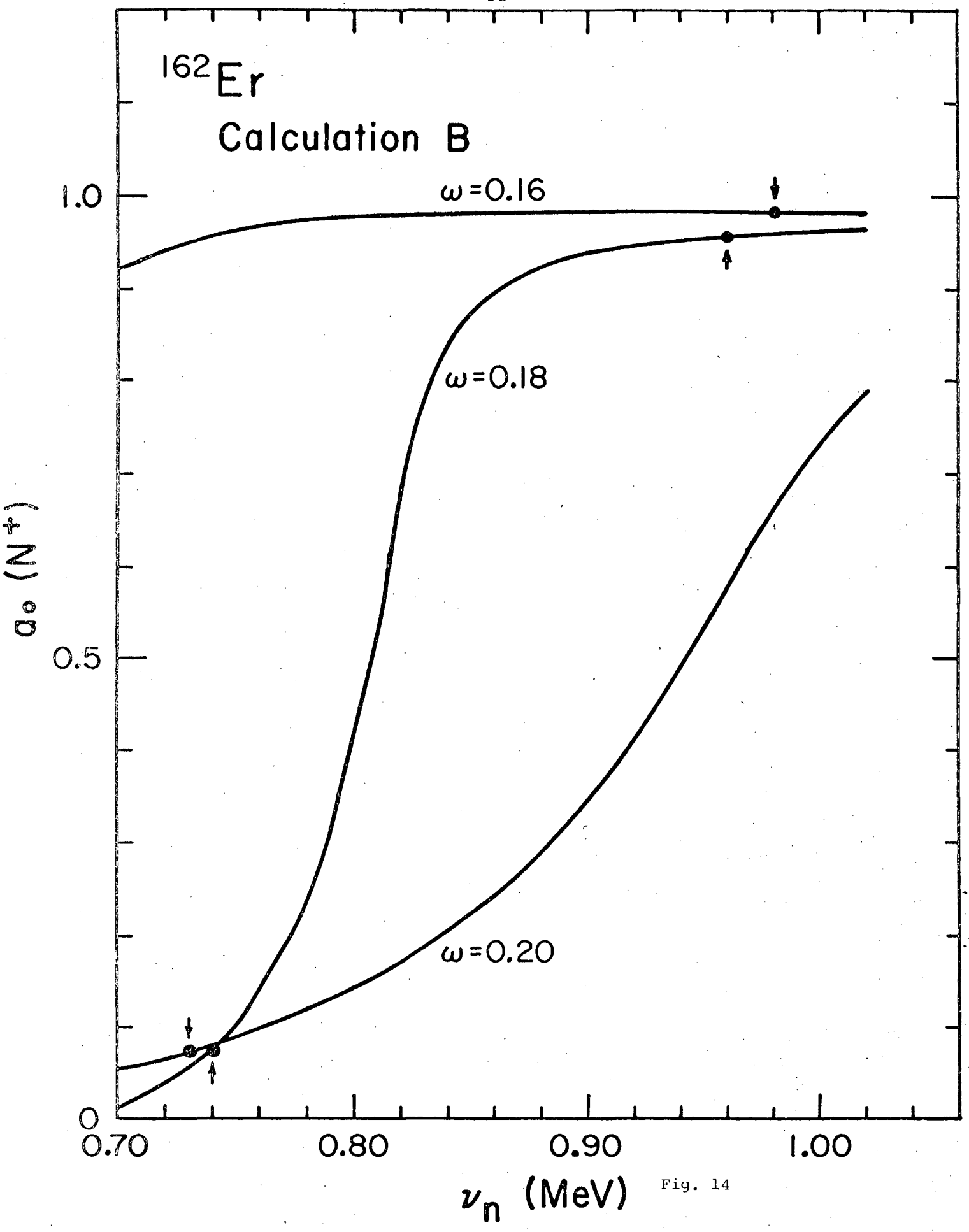
^{162}Er
Calculation B
ω=0.16
ω=0.18
ω=0.20
1.0
0.5
0
$a_\circ$ (N^{-1})
0.70
0.80
0.90
1.00
ν_n (MeV)

Fig. 14

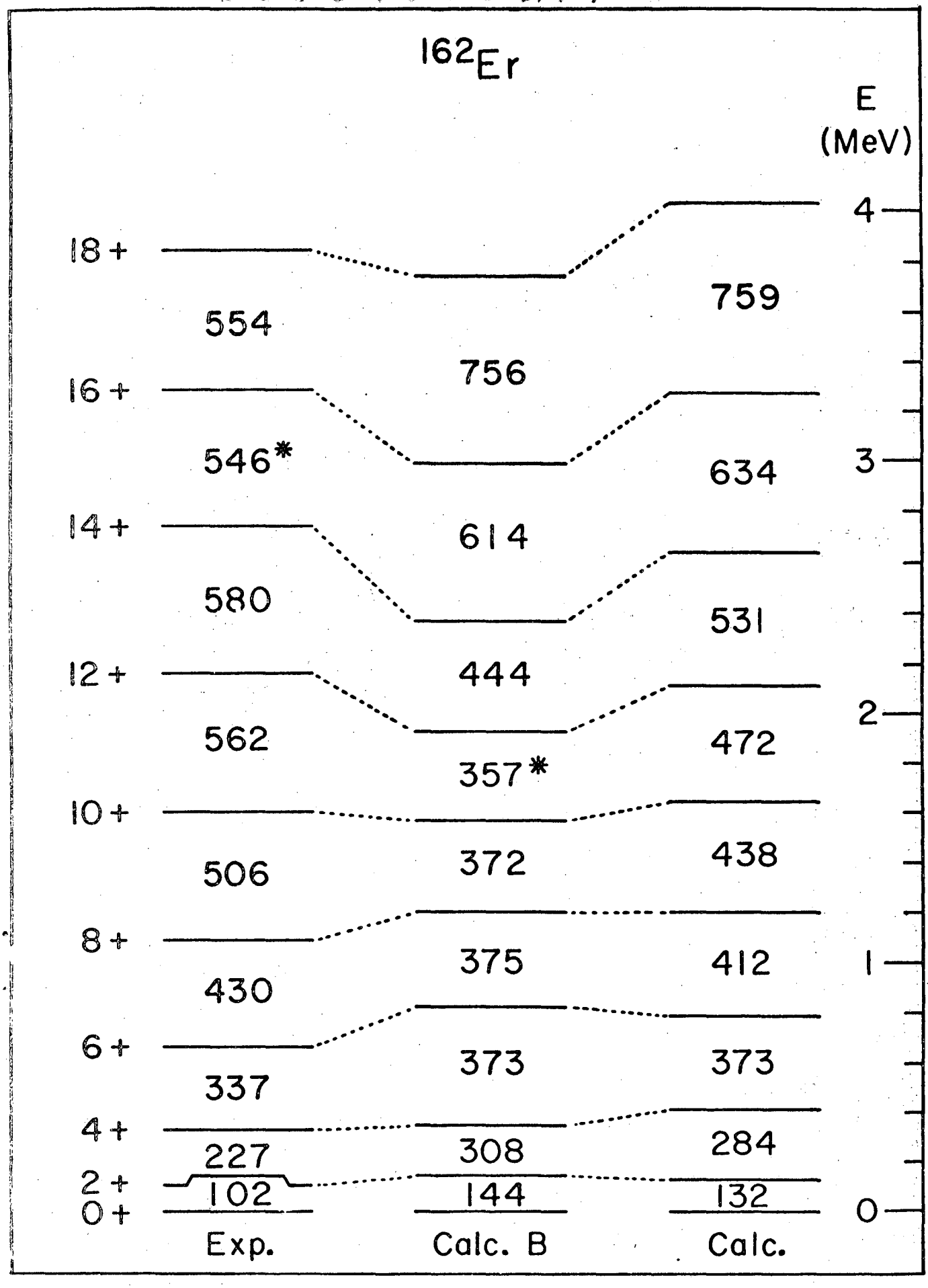
162Er
E (MeV)
4
3
2
1
0
18+
16+
14+
12+
10+
8+
6+
4+
2+
0+
554
546*
580
562
506
430
337
227
102
Exp.
759
756
634
614
531
444
472
357*
438
372
412
375
373
373
308
284
144
132
Calc. B
Calc.

Fig. 15

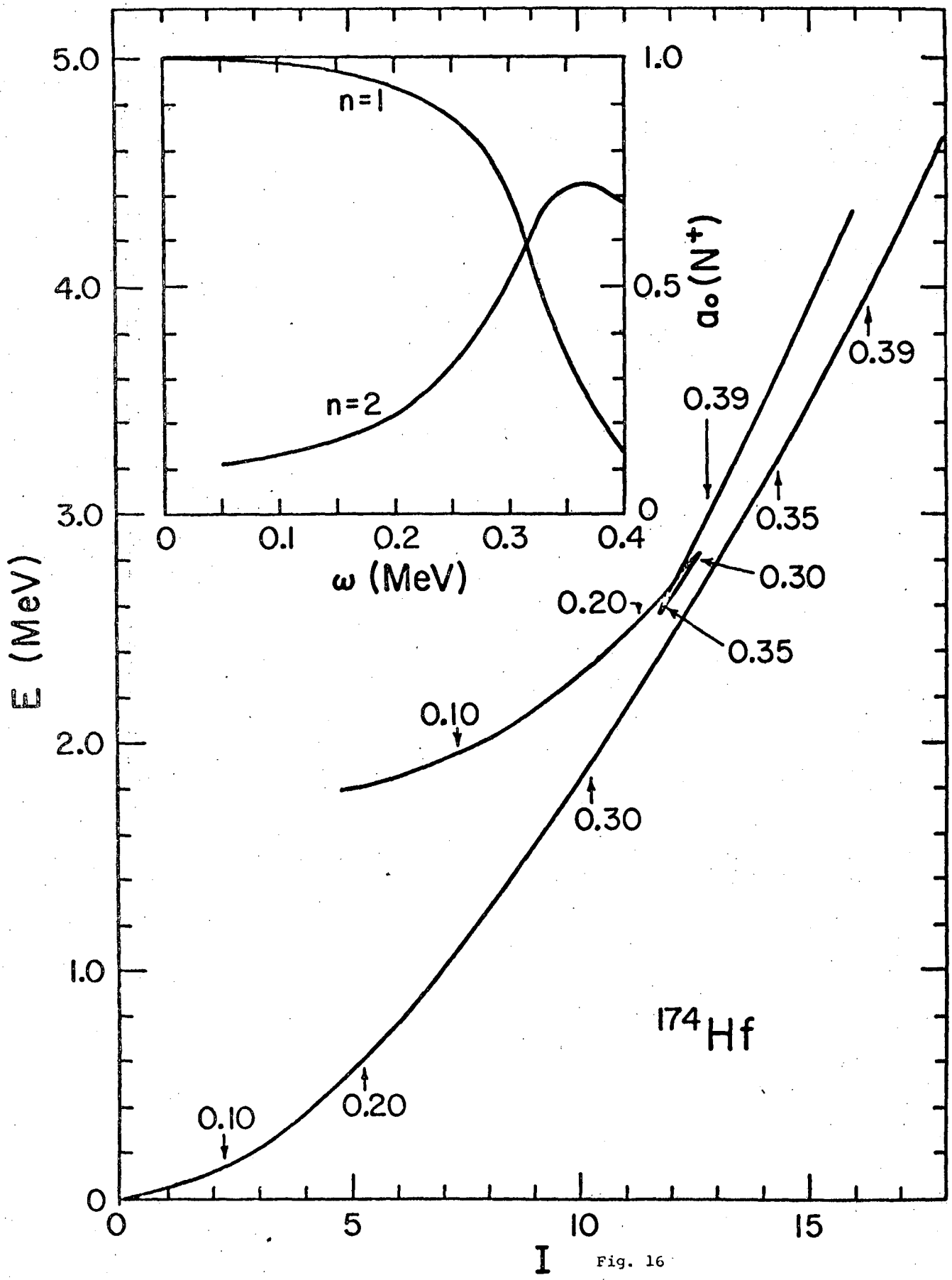
5.0
4.0
3.0
2.0
1.0
0
E (MeV)
0
5
10
15
I
1.0
0.5
0
$a_0(N^+)$
n=1
n=2
0
0.1
0.2
0.3
0.4
ω (MeV)
0.10
0.20
0.30
0.35
0.39
0.39
0.35
0.30
0.20
0.10
0.30
^{174}Hf

Fig. 16

TECHNICAL INFORMATION DIVISION
LAWRENCE BERKELEY LABORATORY
UNIVERSITY OF CALIFORNIA
BERKELEY, CALIFORNIA 94720